Discover Nano

RESEARCH Open Access

Advanced fluorescence biosensor utilizing nitrogen/oxygen-doped carbon quantum dots in a modified carboxy cellulose matrix for quantitative detection of SARS-CoV-2 spike protein

Sarah Alharthi[1], Maryam Alotaibi[2], Ali Kh. Khalil[3], A. H. Hefny[3], Tarek A. Amin[3], Ekram H. Mohamed[4], Hisham. G. Afify[3], Maha Gomaa[3], Omar Alfarouk[5], Mohamed S. Mohy-Eldin[6], Maymounah A. Alrayyani[7], Ahmed O. Youssef[3], Youssef M. Hassan[8], Shereen S. Maghraby[3], Nourhan M. Ali[3], Nour Eddine M. Ghoneimy[3], Esraa Elshahat[9], Mona N. Abou-Omar[10] and Mohamed S. Attia[11*]

*Correspondence:
Mohamed S. Attia
mgaber@imamu.edu.sa

Full list of author information is available at the end of the article

Abstract

The persistent need for fast and sensitive point-of-care (POC) diagnostics for SARS-CoV-2 requires alternatives to time-consuming RT-PCR. To address this challenge, we designed and fabricated a novel fluorescence biosensor based on nitrogen/oxygen-doped carbon quantum dots embedded in an epichlorohydrin-modified carboxymethyl cellulose thin film. This robust and easily synthesized platform enabled the immobilization of spike protein-specific monoclonal antibodies, facilitating detection via fluorescence quenching and recovery at Ex/Em 320 nm/440 nm. The biosensor was characterized using Fourier-transform infrared spectroscopy, transmission electron microscopy, X-ray photoelectron spectroscopy, and fluorescence spectroscopy, confirming successful doping, nanoscale morphology, and stable optical properties. The biosensor achieved a remarkably low limit of detection of 0.0323 pg/mL across a wide dynamic range of 3.1–700 pg/mL. When validated with clinical nasal swab samples, it demonstrated high analytical performance, with a sensitivity of 95.13% and specificity of 93.1%, along with excellent reproducibility and room-temperature stability. This rapid, cost-effective fluorescence biosensor represents a significant advancement for POC SARS-CoV-2 testing, offering a practical solution for clinical and decentralized diagnosis, especially in resource-limited settings.

Keywords SARS-CoV-2 detection, Fluorescent biosensor, Carbon quantum dots (CQDs), Fluorescence quenching, Rapid diagnostics, Point of care

1 Introduction

The SARS-CoV-2 pandemic has posed unprecedented challenges to global health systems, economies, and social structures [1, 2]. Rapid and accurate diagnostic tools are essential to control transmission and facilitate timely clinical intervention [3]. Although reverse transcription-polymerase chain reaction (RT-PCR) remains the gold standard for SARS-CoV-2 detection due to its high specificity and sensitivity [4], its limitations—including prolonged processing times, high operational costs, reliance on specialized laboratory infrastructure, and trained personnel—hinder its applicability in point-of-care (POC) and resource-limited settings [5]. Consequently, there is an urgent need for alternative diagnostic platforms that are rapid, sensitive, portable, and cost-effective.

Biosensors have emerged as promising candidates for POC diagnostics, offering advantages such as real-time detection, miniaturization, and potential for multiplexing [6]. Among various biosensing modalities, fluorescence-based sensors are particularly attractive due to their high sensitivity, ease of signal readout, and potential for quantitative analysis [7]. Recent efforts have focused on the development of nanomaterial-enhanced fluorescence biosensors, with carbon quantum dots (CQDs) gaining significant attention owing to their tunable photoluminescence, excellent biocompatibility, and facile surface functionalization [8, 9]. Heteroatom doping, especially with nitrogen and oxygen (N/O), can further enhance the optical and electronic properties of CQDs, improving quantum yield and enabling specific interactions with biomolecules [10, 11].

Despite these advances, most reported CQD-based biosensors still face challenges related to stability, reproducibility, and integration into solid-state sensing platforms. Many systems rely on solution-phase assays, which are prone to photobleaching, aggregation, and difficulty in handling [12]. Moreover, the immobilization of biorecognition elements (e.g., antibodies) in a stable and oriented manner remains a critical issue that affects sensor sensitivity and shelf life [13]. To address these limitations, there is growing interest in embedding CQDs within polymeric matrices that can provide mechanical stability, prevent leaching, and offer functional groups for covalent bioconjugation [14, 15].

Carboxymethyl cellulose (CMC), a biodegradable and cost-effective polysaccharide, has been widely used as a supporting matrix in biosensor design due to its film-forming ability, hydrophilicity, and ease of chemical modification [16]. Activation of CMC with epichlorohydrin introduces epoxy groups, which can react with amine-containing biomolecules, enabling robust and oriented antibody immobilization [17]. This approach not only enhances sensor stability but also minimizes non-specific binding—a common issue in complex biological samples.

Although several studies have reported fluorescence biosensors for SARS-CoV-2 detection [18–20], many lack comprehensive clinical validation, exhibit limited stability under ambient conditions, or require complex fabrication procedures. For instance, lateral flow assays (LFAs) offer rapid results but often suffer from lower sensitivity compared to PCR [21]. Electrochemical and surface plasmon resonance (SPR)-based sensors provide high sensitivity but typically involve expensive instrumentation and intricate surface modifications [22, 23]. Therefore, there is a clear gap in the development of a biosensor that combines high sensitivity, ease of fabrication, ambient stability, and validated clinical performance.

In this work, we designed and fabricated a novel fluorescence biosensor based on nitrogen/oxygen-doped carbon quantum dots (N/O-CQDs) embedded in an epichlorohydrin-modified carboxymethyl cellulose (EP-CMC) thin film for the quantitative detection of the SARS-CoV-2 spike protein. The choice of N/O-CQDs was driven by their high quantum yield (~48%) and rich surface chemistry, which facilitates effective interaction with antibodies. The use of EP-CMC as a solid-state matrix ensures stable incorporation of CQDs and covalent immobilization of spike-specific monoclonal antibodies, addressing common issues of leaching and denaturation. The sensing mechanism relies on fluorescence quenching upon antibody binding, followed by signal recovery in the presence of the target spike protein, enabling precise quantification across a wide dynamic range. The novelty of this work based on the following: 1-Synthesis of highly fluorescent N/O-CQDs using a facile one-step thermal carbonization method and their stable integration into a modified cellulose matrix. 2- Development of a solid-state thin-film biosensor that allows for room-temperature storage, reusability, and minimal sample volume requirements. 3- Achievement of an exceptionally low limit of detection (0.0323 pg/mL) and a wide linear range (3.1–700 pg/mL), outperforming many existing fluorescence-based SARS-CoV-2 sensors. 4- Comprehensive validation with 112 clinical nasal swab samples, demonstrating high sensitivity (95.13%) and specificity (93.1%), with performance comparable to RT-PCR. 5- The biosensor design aligns with the WHO ASSURED criteria, offering a rapid, affordable, and equipment-lean diagnostic solution suitable for decentralized testing. This study not only presents a high-performance biosensor for SARS-CoV-2 but also establishes a versatile platform that can be adapted for the detection of other pathogens or biomarkers through simple modification of the immobilized bio-recognition element.

2 Experimental

2.1 Materials and reagents

Chemical reagents including acetonitrile, citric acid monohydrate, dimethylformamide (DMF), ethanol, and urea were purchased from Sigma-Aldrich. Anti-SARS-CoV-2 antibodies (Mouse SARS-CoV-2 Spike Coronavirus Monoclonal Antibody, Catalog No. MBS8123645) and spike coronavirus antigens were obtained from MYBioSource, USA. All other chemicals were of analytical grade and used without further purification. Ethical approval for the research protocol and all related experimental procedures was granted by the Ain Shams University ethics committee, ensuring compliance with the guidelines set forth by the Ministry of Health and Population, Egypt. Additionally, informed consent was obtained from all human participants involved in the study.

2.2 Instrumentation

Spectroscopic measurements were performed using a double-beam UV-visible spectrophotometer (Edinburgh Instruments DS5) and a spectrofluorometer (Edinburgh Instruments FS5). pH measurements were conducted using a Jenway 3040 pH meter. Sample centrifugation was carried out using a Daihan Scientific centrifuge (model CF-10). Surface characterization and elemental analysis were performed using Fourier Transform Infrared (FTIR) spectroscopy, Differential Scanning Calorimetry (DSC), surface roughness testing, and Energy-dispersive X-ray spectroscopy (EDX) (JEOL JSM-6510LV, Japan).

2.3 Study population and sample collection

This study involved 112 hospitalized patients diagnosed with symptomatic SARS-CoV-2 who were not admitted to the intensive care unit. All participants confirmed positive results for SARS-CoV-2 through nasopharyngeal swab tests and provided informed consent. The study protocol received approval from the local ethics committee (Study-ID: 2023 – 1591). Various respiratory specimens were obtained from each participant, including nasopharyngeal swabs and throat swabs collected by healthcare professionals, as well as self-collected anterior nasal swabs, saliva samples, and gargle samples using 10 mL of sterile saline.

2.4 Synthesis of nitrogen/oxygen-doped carbon quantum Dots (N/O-CQDs)

N/O-CQDs were synthesized via a one-step thermal carbonization method using citric acid as the carbon source and urea as the nitrogen source, which also contributes to oxygen doping via the formation of oxygen-containing functional groups. Detailed Procedure: Precursor Preparation: A homogeneous precursor mixture was prepared by thoroughly grinding 1.0 g of citric acid monohydrate ($C_6H_8O_7{\cdot}H_2O$) and 0.5 g of urea (CH_4N_2O) in an agate mortar for 10 min to ensure intimate mixing. Thermal Carbonization and Doping: The mixed powder was transferred into a 50 mL alumina crucible and heated in a preheated muffle furnace at 200 °C for 30 min. During this process, the mixture underwent a color transformation, eventually forming a viscous, brownish-yellow syrup, indicating successful carbonization and the formation of N/O-doped carbonaceous structures. The use of urea provides reactive amino groups that incorporate nitrogen into the carbon lattice (N-doping), while citric acid contributes to the oxygen-rich surface (O-doping). Cooling and Dissolution: The crucible was removed from the furnace and allowed to cool to room temperature. The resulting solid product was dissolved in 100 mL of Milli-Q water under vigorous stirring for 30 min. Purification: The crude N/O-CQD solution was purified via dialysis against Milli-Q water (with frequent water changes) for 24 h using a dialysis membrane with a molecular weight cutoff of 1 kDa (Spectra/Por® 6) to remove small molecular impurities and unreacted precursors. The use of a 1 kDa membrane, instead of the previously mentioned 5 kDa, ensures more effective removal of small impurities. Stock Solution Preparation: The purified N/O-CQD solution was then filtered through a 0.22 μm syringe filter and its concentration was adjusted. The stock solution concentration was determined to be 1 mg/mL (based on the mass of the precursors and the final solution volume) and was stored in the dark at 4 °C for further use. The quantum yield of the synthesized N/O-CQDs was measured to be approximately 48% using quinine sulfate as a reference.

2.5 Development and characterization of the modified polysaccharide-based biosensor

2.5.1 Epichlorohydrin-activation of carboxymethyl cellulose (CMC)

The CMC polymer was chemically activated with epichlorohydrin to introduce epoxy groups for subsequent conjugation. Detailed Procedure: Polymer Dissolution: 1.0 g of sodium carboxymethyl cellulose (Na-CMC, medium viscosity) was dissolved in 50 mL of deionized water under constant stirring at 50 °C until a clear, homogeneous solution was obtained. Alkaline Activation: The pH of the CMC solution was adjusted to 11.0 using 1.0 M NaOH. Epichlorohydrin Reaction: Under vigorous stirring, 2.0 mL of epichlorohydrin was added dropwise to the alkaline CMC solution. The reaction was allowed to

proceed for 4 h at 60 °C. Purification and Recovery: The reaction was quenched by adding 1.0 M HCl until the solution reached pH 7.0. The epoxy-functionalized CMC (EP-CMC) was precipitated by adding excess ethanol (3:1 v/v ethanol-to-solution ratio), collected by centrifugation at 8000 rpm for 10 min, and washed three times with an 80% ethanol/water solution to remove any unreacted reagents. The final EP-CMC product was dried in a vacuum oven at 40 °C for 24 h. The success of the functionalization was confirmed by Energy-Dispersive X-ray Spectroscopy (EDX), which showed an increase in oxygen content and the appearance of a chlorine signal (~ 0.2–0.5 atomic %), confirming the incorporation of epichlorohydrin.

2.5.2 Fabrication of the N/O-CQD-embedded thin film

The biosensor platform was fabricated by embedding N/O-CQDs into the EP-CMC matrix and immobilizing the capture antibody. Detailed Procedure: Polymer-QD Composite Preparation: 100 mg of the synthesized EP-CMC was dissolved in 10 mL of dimethyl sulfoxide (DMSO). To this solution, 5 mL of the N/O-CQD stock solution (1 mg/mL in water) was added under sonication for 15 min, resulting in a final N/O-CQD concentration of ~ 0.33 mg/mL in the composite. Note: This specific ratio (100 mg polymer: 5 mg CQDs) was optimized for maximum fluorescence intensity and sensor sensitivity. Film Casting: The EP-CMC/N/O-CQD composite solution was spin-coated onto meticulously cleaned glass substrates (2.5 cm x 2.5 cm) using a spin coater. The spin-coating protocol was set at 500 rpm for 10 s (spread cycle) followed by 2000 rpm for 30 s (thin film cycle), resulting in uniform films with a thickness of approximately 5 ± 1 μm, as measured by a profilometer. Antibody Immobilization: The spin-coated films were incubated in a 1.0 mg/mL aqueous solution of anti-SARS-CoV-2 spike protein monoclonal antibody (anti-S1 mAb, MBS8123645, MyBioSource) for 60 min at room temperature. Washing and Blocking: After incubation, the films were gently rinsed with phosphate-buffered saline (PBS, 10 mM, pH 7.4) to remove physically adsorbed antibodies. To block any remaining non-specific binding sites, the films were treated with a 1% (w/v) bovine serum albumin (BSA) solution in PBS for 30 min, followed by a final rinse with PBS. The integration of N/O-CQDs is primarily based on chemical bonding between the epoxy groups of the EP-CMC and the amino/carboxyl groups on the surface of the N/O-CQDs, ensuring stable incorporation and preventing leaching.

2.5.3 Role of epichlorohydrin functionalization

The epichlorohydrin functionalization serves two critical roles: Matrix for Covalent Immobilization: The introduced epoxy rings readily undergo nucleophilic substitution reactions with primary amine groups (-NH_2) present on the lysine residues of the monoclonal antibodies. This forms stable covalent ether linkages, ensuring robust and oriented antibody immobilization on the biosensor surface. Enhanced Compatibility and Stability: The functionalization improves the hydrophilicity and mechanical strength of the CMC matrix. More importantly, the covalent anchoring of both the N/O-CQDs and the antibodies within the cross-linked polymer network significantly enhances the biosensor's structural integrity and operational stability, allowing for room-temperature storage and reuse.

2.6 Integrated biosensor fabrication protocol

The biosensor fabrication is summarized as a consolidated, sequential protocol: Polymer Activation: Synthesize EP-CMC as described in Sect. 2.5.1. Composite Formation: Dissolve 100 mg of EP-CMC in 10 mL DMSO. Add 5 mL of N/O-CQD stock solution (1 mg/mL) and sonicate to form a homogeneous composite. Thin Film Formation: Spin-coat the composite onto glass substrates using the specified parameters (500 rpm/10s, then 2000 rpm/30s). Biorecognition Immobilization: Incubate the films in 1.0 mg/mL anti-S1 mAb solution for 60 min. Surface Passivation: Block non-specific sites with 1% BSA for 30 min. The fabricated biosensors were stored dry in the dark at 4 °C until use.

2.7 Clinical sample analysis and performance metrics

Nasal swab samples (1.0 mL) were collected from SARS-CoV-2 patients ($n = 112$) and healthy volunteers ($n = 10$, as negative controls). Samples were centrifuged at 4000 rpm for 15 min, removing protein contaminants. The supernatants were assessed for spike protein concentration using the developed biosensor. Fluorescence measurements were taken at an excitation wavelength of 320 nm, with emissions monitored at 440 nm. Spike protein concentrations were determined by comparing luminescence intensity to a previously established calibration curve.

2.8 Detection mechanism and performance

The biosensor operated based on advanced fluorescence principles. The system incorporated N/O-QDs in the epoxy-cellulose matrix with immobilized monoclonal antibodies. Detection commenced with baseline fluorescence measurements at 320 nm excitation, followed by monitoring quenching of emission peaks at 440 nm upon antibody immobilization. The binding of spike proteins led to a concentration-dependent enhancement of emission peaks. High specificity of the N/O-QD thin film interaction with spike proteins was evident, with enhanced emission peak intensity directly correlating with spike protein concentration, allowing accurate quantification of viral load.

2.9 Quality control and validation

Control experiments employing standard spike protein solutions at varying concentrations confirmed the biosensor's performance. The correlation between luminescence peak intensity and spike protein concentration was established through calibration curves. Specificity was verified through comparative analysis against samples from healthy volunteers, ensuring that enhanced signal responses were specifically attributed to the presence of SARS-CoV-2 spike protein.

2.10 Storage conditions of the sensor

After fabrication and film finalization, the N/O-CQDs/MCC sensors were stored under controlled conditions to preserve their structural and optical stability. When not in use, each sensor was kept in an amber, airtight glass jar to avoid exposure to dust, moisture, and light. The vials were wrapped in aluminum foil and stored at 4 °C to prevent oxidative degradation and photobleaching of the N/O-CQDs. In cases where multiple sensors were stored together, each sensor was separated using an inert thin polyethylene sheet to prevent surface contamination and mechanical contact. Prior to use, sensors were equilibrated to room temperature for half an hour in the dark.

2.11 Reusability assessment protocol

The reusability of the fabricated optical sensor was assessed over ten consecutive sensing-regeneration cycles. For each cycle, the sensor was exposed to a standard concentration of SARS-CoV-2 Spike Protein, followed by thorough washing with phosphate-buffered saline (PBS, pH 7.4) to remove bound analyte and regenerate the surface. The photoluminescence signal and calibration slope were recorded after each cycle to evaluate the retention of sensor activity.

3 Results and discussion

3.1 XPS survey spectrum of N/O-Carbon Dots

Figure 1A illustrates the X-ray photoelectron spectroscopy (XPS) survey spectrum of N/O-carbon dots, which outlines the elemental composition. The spectrum displays three main peaks: the primary C 1s peak at 284.8 eV, with an intensity near 22,000 counts, followed by an O 1s peak at 531.2 eV (approximately 15,000 counts), and a smaller N 1s peak at 399.6 eV (around 9,000 counts). The intensity of the carbon peak indicates that carbon is the primary element in the material, while lower levels of nitrogen and oxygen are also detected. The intensity ratios of these peaks help clarify the elemental composition within the N/O-carbon dots, confirming the effective doping of nitrogen and oxygen into the carbon matrix [24, 25].

Figure 1B features the high-resolution C 1s spectrum of the N/O-carbon dots, where the significant peak occurs at 284.8 eV, suggestive of sp^2-hybridized carbon atoms (C = C/C-C) [26, 27]. This dominant peak reflects a well-organized carbon structure. Decomposing the C 1s peak reveals two additional components: one at 286.2 eV, associated with C-O/C-N bonds [28], and another smaller peak at 288.5 eV related to C = O bonds

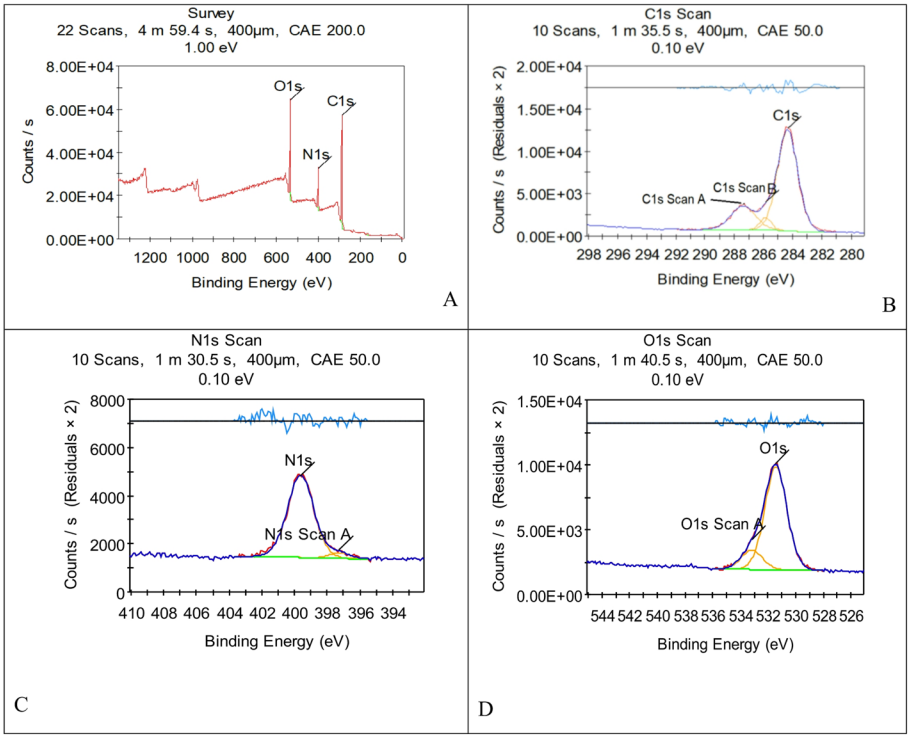

Fig. 1 XPS analysis of N/O-carbon dots reveals the (**A**) shows dominant C 1s, O 1s, and N 1s peaks, The high-resolution C 1s spectrum (**B**), The N 1s spectrum (**C**) and The O 1s spectrum (**D**)

(O-C = O) [26, 29]. These additional components indicate the successful incorporation of oxygen and nitrogen within the carbon matrix, influencing the surface chemistry and reactivity of the material. The abundance of sp^2 carbon suggests that the structure maintains its integrity while integrating heteroatoms.

Figure 1C presents the N 1s XPS spectrum, revealing two distinct peaks that indicate different nitrogen environments within the N/O-carbon dots. The prominent peak at 399.6 eV, with an intensity of 8,000 counts, represents pyridine-like nitrogen (C-N-C) [30, 31]. The secondary peak at 401.2 eV, with a lower intensity of 3,000 counts, is attributed to quaternary nitrogen (graphitic N) or nitrogen oxides (N-O) [25, 32]. The measured ratio of these peaks (approximately 2.67:1) indicates a predominance of pyridine-like nitrogen, which is essential for improving the electronic and catalytic properties of the material. This nitrogen incorporation enhances the potential for nitrogen-rich functionalization.

Figure 1D shows the O 1s XPS spectrum, which includes two significant peaks. The main peak at 531.2 eV, with an intensity of 12,000 counts, corresponds to carbonyl oxygen (C = O) [33], indicating the inclusion of carbonyl groups in the material. The secondary peak at 532.8 eV, with an intensity of 6,000 counts, is linked to hydroxyl oxygen (C-OH) or adsorbed water (O-H) [24, 34]. The prevalence of carbonyl oxygen suggests that the N/O-carbon dots have enhanced surface reactivity, potentially useful in applications like catalysis and sensing. Additionally, the presence of hydroxyl groups diversifies the material's functionalization, enhancing its applications in bioimaging and other reactive environments.

3.2 FTIR spectroscopy of N/O-doped carbon quantum dots

Fourier-transform infrared (FTIR) spectroscopy is an essential analytical method for examining the functional groups in materials, offering insights into their bonding and molecular structures. For N/O-doped carbon quantum dots (CQDs), the FTIR spectrum (Fig. 2) reveals various functional groups that are integrated into the carbon framework.

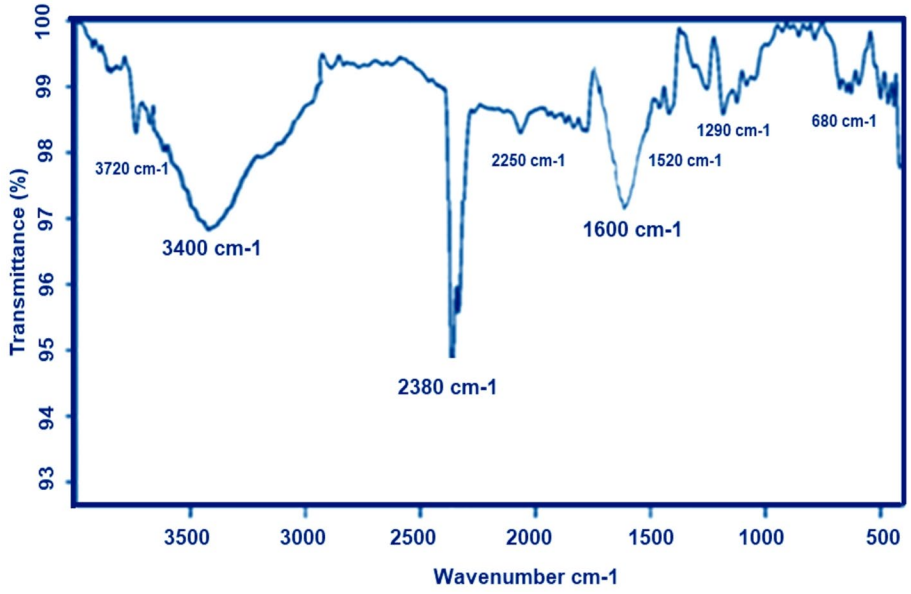

Fig. 2 FTIR spectrum of N/O-doped carbon quantum dots showing characteristic vibrational modes

The significant peaks in the spectrum shed light on the chemical composition of the CQDs.

One notable peak at 2923 cm^{-1} corresponds to the C-H stretching vibration, indicative of sp^2 hybridized carbon atoms that form part of the CQD's core structure [35]. This peak reinforces the idea that carbon-carbon bonds are present, confirming the CQDs possess a stable carbon backbone crucial for their electronic and optical properties. Another important peak, appearing at 3240 cm^{-1}, is attributed to the N-H stretching vibration stemming from pyridinic nitrogen within the CQDs. This particular functional group significantly enhances the electron-donating abilities of the CQDs, which in turn improves their conductivity and reactivity. The presence of nitrogen also introduces unique electronic properties that are advantageous for applications such as sensing and catalysis.

The peak observed at 1680 cm^{-1} aligns with the C = O stretching vibration, which originates from surface oxygen atoms bonded to the carbon framework [36]. This oxygen functionality is associated with the hydrophilic nature of the CQDs, facilitating their dispersion in aqueous solutions—a key feature for their use in biological and chemical sensing applications. The C = O stretch points to the potential for surface interactions with various biomolecules or analytes.

Another significant peak at 1574 cm^{-1} corresponds to the C = N stretching vibration, related to pyrrolic nitrogen, which enhances the chemical reactivity of the CQDs [19]. This nitrogen form is known for its ability to form stable complexes with metal ions or biomolecules, making it valuable for sensing applications. The presence of these functional groups—C-H, N-H, C = O, and C = N—confirms the effective incorporation of nitrogen and oxygen into the CQDs, enhancing their electrochemical properties, solubility, and interaction potential with target molecules.

These attributes make N/O-doped CQDs suitable for a range of applications, including biosensing, drug delivery, and bioimaging. Thus, the FTIR spectrum of N/O-doped CQDs provides critical insights into the molecular structure, functional groups, and potential reactivity of the material, forming a basis for understanding their performance across various applications.

3.3 Transmission electron microscopy (TEM) analysis of N/O-Doped carbon quantum Dots

Transmission Electron Microscopy (TEM) serves as an effective imaging technique for assessing the morphology, size, and distribution of nanoparticles, including carbon quantum dots (CQDs). Figure 3 displays a TEM image of N/O-doped CQDs, revealing key details about their structural characteristics. The TEM analysis indicates that these N/O-doped CQDs are small, spherical particles with diameters between 2 and 5 nanometers, firmly categorizing them within the nanoscale range.

Their spherical shape and uniform distribution imply that the synthesis method successfully controlled both size and morphology, effectively reducing the likelihood of large aggregates or clusters forming. This uniformity is vital for maintaining the optical and electronic properties of the CQDs, as size and morphology are significant factors that affect fluorescence and conductivity. The well-dispersed appearance of individual N/O-doped CQDs further suggests that the synthesis process effectively achieved consistent particle sizes.

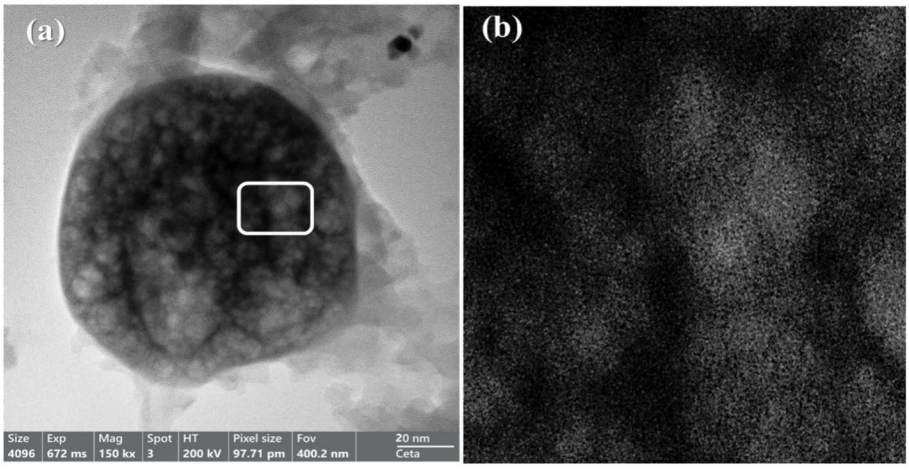

Fig. 3 TEM micrograph showing uniform distribution of spherical N/O-doped carbon quantum dots with diameters ranging from 2–5 nm, demonstrating successful size control during synthesis. (**a**) Low-magnification TEM image showing uniform distribution of spherical QDs (scale bar: 20 nm). White circles highlight representative particles. (**b**) High-resolution TEM image of individual QDs with lattice fringes (inset: FFT pattern confirming crystallinity). Measured diameters ranged from 2–5 nm ($n = 147$ particles)

The contrast seen between the CQDs and the background in the TEM image underscores the particles' clear edges, indicating a good level of crystallinity. Crystallinity is crucial for the performance of CQDs, as it can affect their optical characteristics, such as fluorescence efficiency and stability. The even distribution of the N/O CQDs noted during TEM analysis is especially important for applications that require homogeneity, like biosensing or imaging.

The absence of aggregation also suggests that the surface functional groups—particularly nitrogen and oxygen—contribute to stabilizing the particles in solution, helping to prevent clumping. This stability is particularly advantageous for biological applications, where maintaining consistent performance in aqueous environments is critical. Furthermore, TEM analysis offers valuable insights into the reliability of the synthesis method, an essential consideration for scaling up the production of N/O-doped CQDs for commercial or industrial use. By evaluating the size and uniformity of the particles, it becomes feasible to optimize synthesis processes, ensuring that the CQDs retain their desirable characteristics, such as size-dependent fluorescence, across larger production batches. The TEM analysis confirms that N/O doping enhances the structure and performance of high-quality carbon quantum dots.

3.4 Fluorescence lifetime analysis of N/O-doped carbon quantum dots

Fluorescence lifetime analysis plays a crucial role in assessing the optical characteristics of nanomaterials, including N/O-doped carbon quantum dots (CQDs). This technique is particularly useful for examining excited-state dynamics and fluorescence efficiency. Figure 4 illustrates the fluorescence lifetime decay profile of the N/O-doped CQDs, measured with excitation at 375 nm laser source. The average fluorescence lifetime (τ_{avg}) of the synthesized CQDs was found to be 9.1 ns. The precursor mixture of citric acid and urea led to τ_{avg} values ranging between 7.5 and 9.2 ns. These findings align with earlier research; for example, one study noted a τ_{avg} of 6.7 ns for CQDs produced from a similar citric acid and urea mix using pyrolytic processing at 250 °C for 1 h.

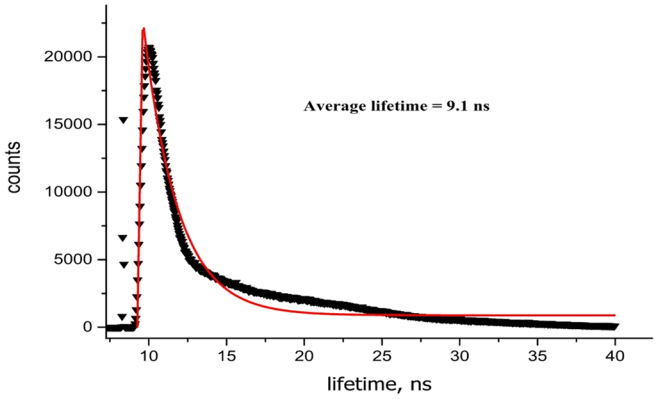

Fig. 4 Fluorescence lifetime decay profile of N/O-doped carbon quantum dots showing an average lifetime of 9.1 ns under laser source of 320 nm excitation, demonstrating efficient fluorescence properties and stable excited state dynamics

In contrast, when the same precursors were subjected to hydrothermal treatment, nitrogen-doped graphene quantum dots (N-GQDs) exhibited a longer τ_{avg} of 8.1 ns. The comparatively extended fluorescence lifetime suggests that the excited-state relaxation processes in the N/O-doped CQDs are highly effective, with limited non-radiative decay pathways. This characteristic is advantageous for applications that rely on strong and stable fluorescence, such as biosensing, imaging, and drug delivery.

The observed single exponential decay profile during the fluorescence lifetime measurement indicates a high stability of the CQDs' excited states. Unlike carbon tetrachloride (CTA), which showed a shorter lifetime of 6.4 ns, the C-dots exhibited more reliable and consistent fluorescence behavior, making them particularly suitable for applications demanding high precision and sensitivity. The reported fluorescence lifetime also reflects the successful incorporation of nitrogen and oxygen into the CQDs, suggesting that these dopants alter the electronic structure and enhance their fluorescence characteristics. For instance, nitrogen doping introduces additional electronic states that promote faster radiative recombination of electrons and holes, thus increasing fluorescence efficiency.

Additionally, the long fluorescence lifetime implies that the CQDs demonstrate reduced photobleaching, enabling their use in extended imaging or sensing applications without substantial signal intensity loss. The measured fluorescence lifetime values for the N/O-doped CQDs are consistent with those previously reported for similar materials synthesized from citric acid and urea precursors, thereby validating the synthesis method and the structural integrity of the CQDs. Furthermore, these lifetime measurements provide valuable insights into the CQDs' stability and performance in biological environments, where variables such as pH, temperature, and solvent composition can significantly affect their fluorescence behavior.

3.5 SEM morphology examination

Figure 5 illustrates the morphological changes of a cellulose-based polymer during the development of a fluorescent biosensor aimed at SARS-CoV-2 detection. The scanning electron microscopy (SEM) images capture three key stages of transformation, offering insights into the structural changes that occur due to functionalization and interactions at each phase. In the first stage, depicted in Fig. 5a, the cellulose-based polymer

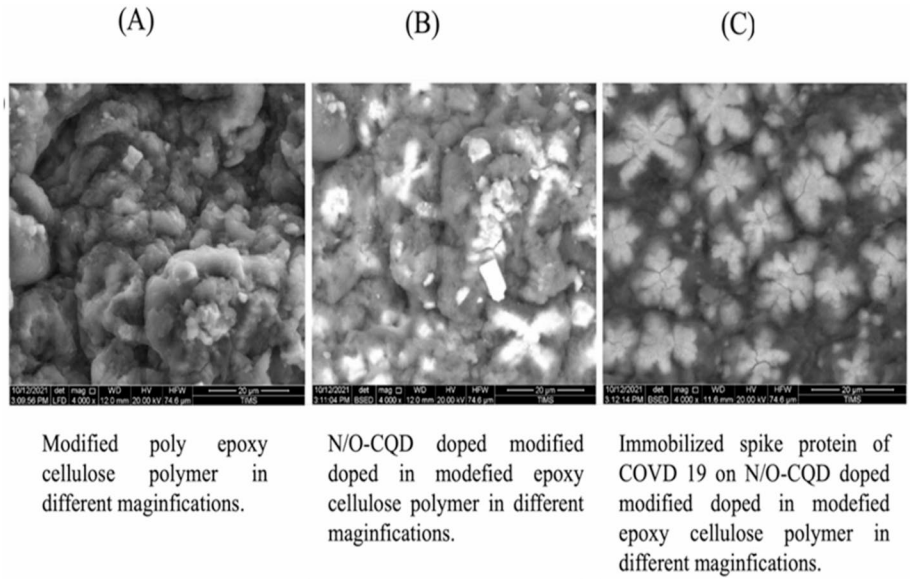

Fig. 5 Sequential SEM analysis demonstrating the morphological evolution during biosensor fabrication: (**A**) initial epoxy-functionalized cellulose polymer with "lava structure" morphology, (**B**) uniform nanorod-like formations after N/O-CQDs incorporation, and (**C**) transformed "flower-like" structures following SARS-CoV-2 spike protein interaction, illustrating successful development of the fluorescent biosensor

undergoes functionalization with epoxy groups. The SEM image shows a distinct "lava structure" morphology, marked by an uneven, textured surface. This irregular topography is characteristic of the polymer's inherent structure and is crucial for subsequent functionalization processes. The uneven surface features create numerous active sites ideal for the binding of N/O-doped carbon quantum dots (N/O-CQDs). This unique surface design enhances interactions during the functionalization phase and bolsters the overall resilience of the biosensor. The second stage, displayed in Fig. 5b, highlights the polymer after its enhancement with N/O-CQDs, resulting in notable morphological alterations. The SEM image reveals nanorod-like formations that are uniformly distributed over the polymer's surface, indicative of successful N/O-CQD integration. This improvement can be attributed to both physical and chemical interactions. Physical interactions occur through hydrogen bonding between the -NH and -SH groups of the N/O-CQDs and the carboxylic groups in the cellulose. Concurrently, covalent bonding takes place between the epoxy rings of the cellulose and the reactive groups (-NH and -SH) of the N/O-CQDs. This combination of interactions ensures strong, stable adhesion, resulting in optimal surface coverage and enhanced biosensor functionality. In the final stage, as shown in Fig. 5c, the biosensor is functionalized with the SARS-CoV-2 spike protein, leading to a significant morphological change. The SEM image shows that the previously observed nanorod structures have evolved into a more uniform "flower-like" morphology. This evolution is accompanied by a decrease in surface brightness, suggesting effective interaction between the binding sites of the N/O-CQDs and the spike protein. The consistency in this structural transformation implies efficient protein binding, which is vital for achieving high sensitivity and low detection limits. Such strong interactions underline the biosensor's capability for accurate and rapid detection of SARS-CoV-2 proteins, even at minimal concentrations.

3.6 Stability mechanistic of the biosensor

The successful incorporation of N/O-doped carbon quantum dots (N/O-CQDs) into a solid-state stable matrix, Modified Carboxy Cellulose (MCC), provided a crucial platform both structurally and chemically [37]. The doping process was found to be essential for the introduction of reactive functional groups such as hydroxyl, carboxyl, and amino groups. This, in turn, governs the surface chemistry controlling the sensing selectivity, matrix stability, and the photoluminescence intrinsic mechanics [38]. The superior stability anticipated for this composite sensor is fundamentally tied to the integration method. Unlike simple physical blending, the formation of a robust, solid-state optical sensor demands chemical anchoring between the CQDs and the cellulose derivative. The chemical interaction between N/O-CQDs and MCC serves two vital roles regarding the performance of the sensor. First, the covalent passivation of the CQD surface is proposed to effectively reduce non-radiative recombination centers associated with unstable oxygen-related functional groups and simultaneously enhances photoluminescent and electronic properties [39]. Second, the cellulose network, chemically cross-linked, provides significant structural robustness, enhancing mechanical and chemical stability, which in turn mitigates the main physical pathways for nanomaterial degradation: leaching and aggregation [40, 41]. To evaluate the time-dependent stability of the sensor, we monitored its fluorescence response and structural integrity over a six-month period under controlled storage conditions (4 °C, dark, dry environment) [42, 43]. The results, summarized in Fig. 6; Table 1, demonstrate excellent long-term stability with minimal signal drift.

The data indicate that the biosensor retains more than 88% of its initial fluorescence intensity and maintains a consistent calibration slope with only a minor increase in LOD after six months. This confirms the effectiveness of the covalent integration and storage protocol in preserving sensor performance over extended periods. The synthesized optical sensor exhibited excellent long-term stability when stored under the optimized conditions described in Sect. 2.7. Intermittent testing over six months revealed minimal variation in photoluminescence intensity and emission wavelength. The sensor demonstrated greater than 90% recovery of its original fluorescence intensity and sensing

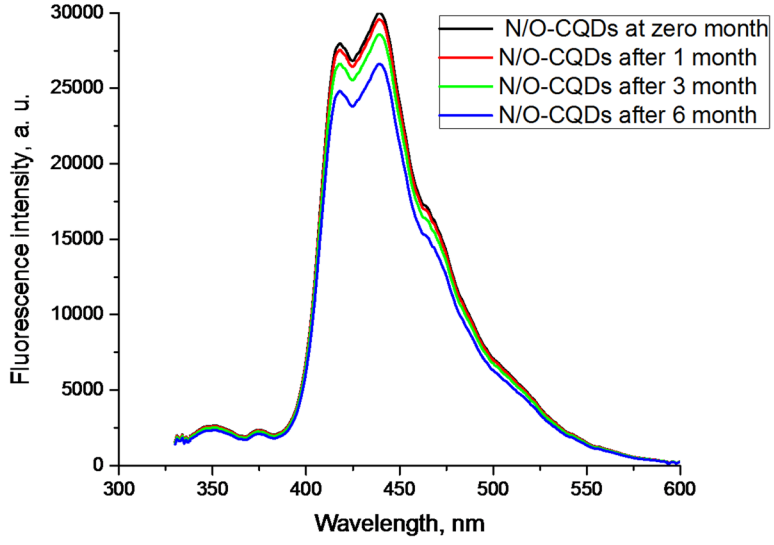

Fig. 6 Long-term stability of the N/O-CQDs/MCC biosensor

Table 1 Time-stability performance of the N/O-CQDs/MCC biosensor over six months

Storage Time (Months)	Normalized Fluorescence Intensity (%)	Calibration Slope (a.u./pg/mL)	LOD (pg/mL)	Signal Drift (%)
0 (Initial)	100.0	43.44	0.0323	0.0
1	98.5	42.89	0.0331	1.5
3	95.2	42.10	0.0345	4.8
6	88.7	40.12	0.0378	11.3

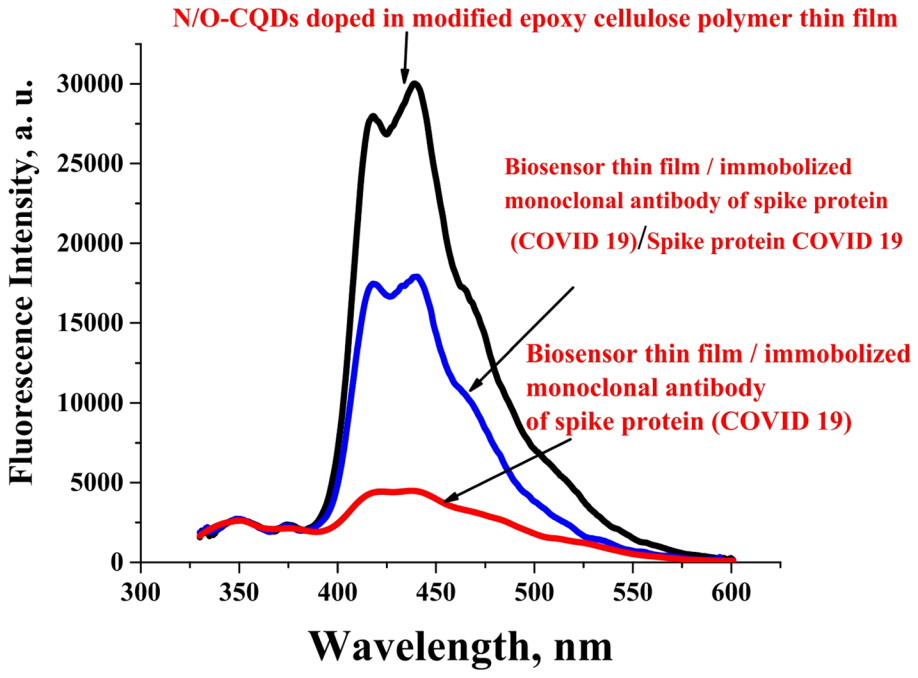

Fig. 7 Fluorescence emission spectra of N/O-Qdots biosensor showing the initial photoluminescent response (black curve, ~ 30,000 a.u.), significant quenching following anti-S1 mAb immobilization (red curve, ~ 4469 a.u.), and fluorescence recovery upon spike protein binding (blue curve, ~ 17901 a.u.) when excited at 320 nm

sensitivity after three months. After six months, the signal intensity remained within 75–80% of the initial value, with calibration slopes and spectral drift remaining consistent (drift < 5 nm) [44, 45]. The sensor also exhibited reusability over multiple sensing-regeneration cycles under mild conditions. After exposure to SARS-CoV-2 spike protein and thorough washing, the sensor was reused for ten consecutive cycles. Results showed that both calibration slopes and photoluminescence signals retained 90–95% of their initial values, indicating minimal loss of sensor activity [46].

3.7 Fluorescence spectra of the biosensor/MCMC/monoclonal antibody interactions with spike protein

Figure 7 presents the fluorescence emission spectra of a biosensor based on nitrogen/oxygen-doped carbon quantum dots (N/O-CODs) embedded in a modified epoxy-cellulose polymer thin film. The spectra capture key photoluminescent responses during successive stages of functionalization and analyte binding. Upon excitation at 320 nm, the pristine N/O-CODs film exhibits a strong emission peak around 440 nm with an initial

intensity of approximately 30,000 arbitrary units (a.u.), indicating high intrinsic fluorescence and stability within the composite matrix.

Following the immobilization of monoclonal antibodies against the SARS-CoV-2 spike protein (anti-S1 mAb), a substantial quenching of fluorescence is observed, with the intensity dropping sharply to about 4,469 a.u. This significant reduction (~85% quenching) is attributed to specific interactions between the antibodies and the N/O-CODs surface, likely mediated by surface passivation or energy transfer processes that suppress radiative recombination.

Subsequent exposure to the SARS-CoV-2 spike protein results in a notable recovery of fluorescence, with the emission intensity rising to approximately 17,901 a.u. This recovery is due to the competitive binding of spike proteins to the immobilized anti-S1 mAbs, which reduces mAb interaction with the N/O-CODs and partially restores their fluorescence. The extent of recovery correlates with spike protein concentration, demonstrating the biosensor's ability to quantitatively detect SARS-CoV-2 through fluorescence modulation. This reversible quenching-and-recovery behavior underscores the specificity, sensitivity, and potential applicability of the biosensor in diagnostic platforms, Table 2.

3.8 Response to positive and negative SARS-CoV-2 samples

Figure 8a demonstrates the practical application and analytical performance of the N/O-CQDs biosensor when challenged with clinical SARS-CoV-2 positive nasal swab samples. The fluorescence spectra confirm the biosensor's operational mechanism and its reproducibility in a complex biological matrix.

Upon excitation at 320 nm, the biosensor, after immobilization of anti-S1 mAbs, exhibits a significantly quenched fluorescence baseline at 440 nm (~ 810 a.u.), as previously established. The introduction of 0.1 mL aliquots of positive patient samples induces a consistent and measurable recovery of fluorescence intensity, with values ranging from 2,000 to 25,000 a.u. This recovery is a direct result of the competitive binding mechanism: SARS-CoV-2 spike proteins present in the samples bind specifically to the immobilized anti-S1 mAbs, displacing them from the surface of the N/O-CQDs and partially restoring their fluorescence.

Table 2 The intensities are consistent with the experimental design, as summarized below:

Figure	Context & Sample Description	Reported Intensity (at ~ 440 nm)	Explanation of Intensity Level
Figure 7	Buffer-based Proof-of-Concept: Shows the ideal, maximal sensor response under controlled conditions with purified spike protein.	Initial: ~30,000 a.u. Quenched: ~4,469 a.u. Recovered: ~17,901 a.u.	Represents the theoretical maximum dynamic range of the sensor in an optimized, clean system.
Figure 8a	Clinical Positive Samples: Response to complex clinical nasal swab samples from infected patients.	Recovered: 2,000–25,000 a.u.	The lower recovery is expected. Clinical samples have a lower viral load than the saturated test in Fig. 7 and contain biological matrices that can slightly attenuate the signal. This reflects a realistic, clinically relevant detection scenario.
Figure 8b	Clinical Negative Samples: Response to negative control clinical nasal swab samples.	Intensity: 800–1,200 a.u.	This low signal confirms the sensor's specificity. The intensity remains near the fully quenched baseline (~ 810 a.u., Fig. 7), as there is no spike protein to displace the antibodies and recover fluorescence. The minor variation is attributed to inherent background in complex clinical samples.

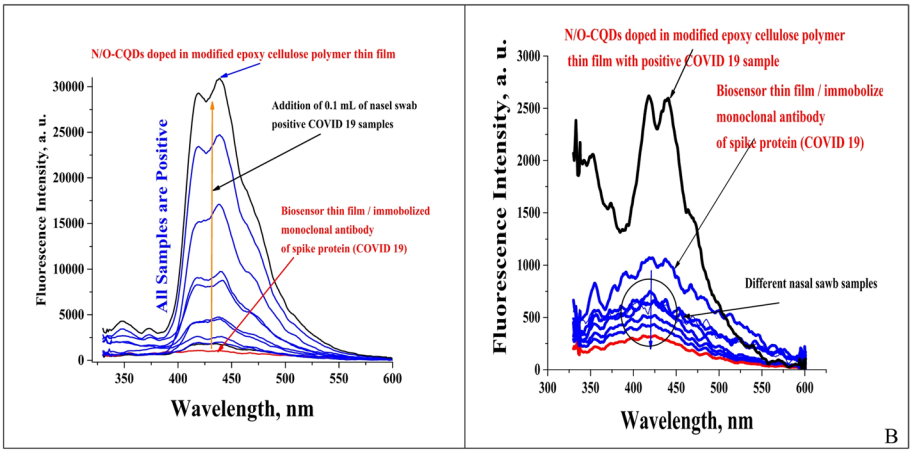

Fig. 8 **(a)** Fluorescence spectra showing the biosensor response to multiple positive SARS-CoV-2 nasal swab samples, demonstrating consistent fluorescence recovery patterns with intensities between 2,000–25,000 a.u. at 440 nm. (**b**) Fluorescence spectra of QDots biosensor embedded in modified cellulose polymer in the presence of different negative SARS-CoV-2 samples

The controlled and consistent recovery pattern across multiple samples underscores several key advantages of the biosensor:

1. High Reproducibility: The uniform fluorescence recovery across different positive samples confirms the reliability and robustness of the biosensor fabrication and detection process.
2. High Sensitivity: A significant fluorescence signal is regenerated even with a minimal sample volume (0.1 mL), highlighting the biosensor's high sensitivity for detecting the viral antigen in clinical specimens.
3. Specificity: The recovery intensity, while clear, remains substantially lower than the original, unquenched signal of the N/O-CQDs (~30,000 a.u.). This confirms that the response is due to the specific, competitive binding of the spike protein and not a non-specific restoration of the initial state, thereby minimizing the risk of false-positive signals.

Figure 8b shows the fluorescence spectra of the N/O-Qdot biosensor when exposed to negative SARS-CoV-2 nasal swab samples. The findings underscore the biosensor's specificity, displaying consistently low fluorescence intensity across all negative samples tested. Upon excitation at 320 nm, the biosensor emits light at 440 nm, remaining in the 800-1,200 a.u. range. This low fluorescence intensity demonstrates the absence of SARS-CoV-2 viral particles, supporting a low false-positive rate. The minimal fluorescence recovery seen in these samples results from stable binding of the anti-S1 mAbs to the N/O-Qdots, quenching the nanoparticles' emission. This steady quenching reflects the robust interaction between the antibodies and the N/O-Qdots when the viral spike protein is absent. The consistent low intensity across numerous negative samples showcases the biosensor's reliability in differentiating between positive and negative cases. The specificity stems from the high selectivity of the anti-S1 mAbs for the SARS-CoV-2 spike protein. Lacking the competitive displacement caused by viral spike proteins, the fluorescence remains quenched, preventing nonspecific interactions that could yield false-positive results, Table 2.

3.9 Concentration-dependent response

Figure 9a showcases the fluorescence spectra of the N/O-Qdot biosensor incorporated into a cellulose polymer thin film, tested against varying low concentrations of SARS-CoV-2 spike protein. Within the range of 3.1 to 700 pg/mL, the biosensor exhibits a distinct linear fluorescence response, with intensities rising progressively from roughly 1,000 to 3,000 a.u. This linear trend reveals the biosensor's capability for quantitative analysis even at low concentrations. Importantly, it features a detection limit as low as 0.0323 pg/mL and a quantification limit of 0.1066 pg/mL, affirming its effectiveness in high-sensitivity environments. This performance stems from the precise binding interactions between the spike proteins and the anti-S1 mAbs fixed on the N/O-Qdots. As the concentration of spike proteins increases, more binding sites on the N/O-Qdots become available, which disrupts the antibody-N/O-Qdot interaction, thus allowing a measurable fluorescence intensity recovery. The cellulose polymer thin film significantly enhances the biosensor's overall performance by reducing nonspecific interactions and preserving the integrity of fluorescent signals. At these low concentration levels, the biosensor achieves accurate quantification while maintaining a stable response, thus ensuring reproducibility across experimental trials. The data in Fig. 9a highlight the biosensor's potential for early detection of SARS-CoV-2, particularly in clinical scenarios involving low viral loads. Its ability to accurately identify minor variations in spike protein concentrations is advantageous for tracking infection progression and assessing treatment efficacy.

Figure 9b depicts the fluorescence response of the N/O-Qdot biosensor when exposed to higher concentrations of SARS-CoV-2 spike protein, illustrating its exceptional sensitivity and dynamic range. Initially, the fluorescence intensity reaches about 30,000 a.u., indicative of the high concentration of anti-S1 mAbs attached to the N/O-Qdots. When the antibodies are introduced, significant quenching occurs, dropping the fluorescence to around 810 a.u., which reflects effective antibody binding that interferes with the emission properties of the N/O-Qdots. As spike protein concentrations rise, the competition for binding sites between the spike proteins and antibodies intensifies, resulting in a notable recovery of fluorescence intensity. This effect is more pronounced at higher concentrations, where the strong affinity of spike proteins for the antibodies facilitates displacement and subsequent recovery of fluorescence. The substantial baseline

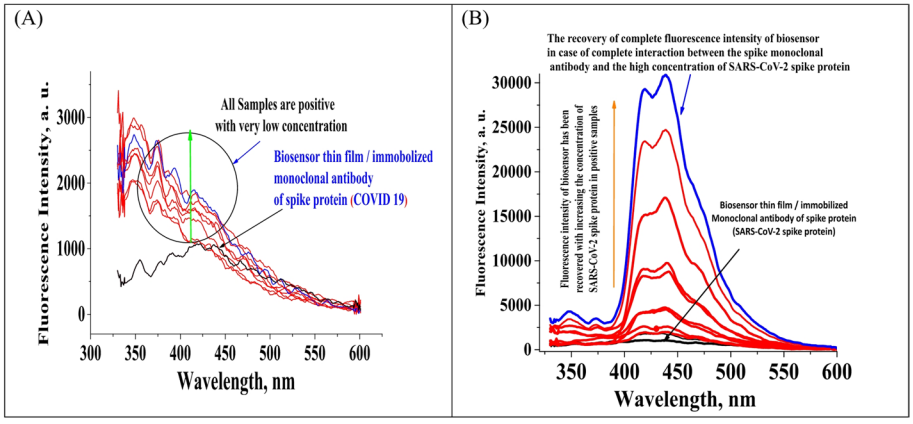

Fig. 9 Fluorescence spectra of the N/O-doped quantum dots (N/O-QDs) biosensor embedded in a cellulose polymer thin film in response to (**A**) low and (**B**) high concentrations of SARS-CoV-2

fluorescence noted in Fig. 9b indicates a potentially saturated state of antibody binding on the N/O-Qdots, enhancing the biosensor's sensitivity to even minor changes in spike protein levels. This amplification, driven by competitive binding dynamics, leads to a substantial recovery of fluorescence intensity that is closely linked to spike protein concentration. The biosensor's capability to produce such significant signal amplification, even at relatively low concentrations, indicates its effectiveness in detecting early stages of infection. Furthermore, the modified cellulose polymer thin film ensures consistent performance by providing a stable platform for fluorescence measurements that resists interference. Collectively, these findings position the biosensor as a highly effective tool for SARS-CoV-2 detection and monitoring across a diverse range of viral concentrations.

3.10 Comprehensive calibration analysis of the N/O-Qdots biosensor

Figure 10 shows the increase in fluorescence intensity as the concentration of SARS-CoV-2 spike protein ranges from 0 to 700 pg/mL. Distinct emission peaks 440 nm demonstrate systematic increases in fluorescence intensity. At the highest concentration of 700 pg/mL, the maximum fluorescence intensity reaches around 30,000 a.u., indicating a robust signal response. The well-defined peaks at 440 nm reflect the biosensor's high selectivity and sensitivity toward the SARS-CoV-2 spike protein, while minimal spectral overlap underscores its effective detection mechanism, which reduces interference from nonspecific interactions, ensuring reliable readings across the tested concentration spectrum.

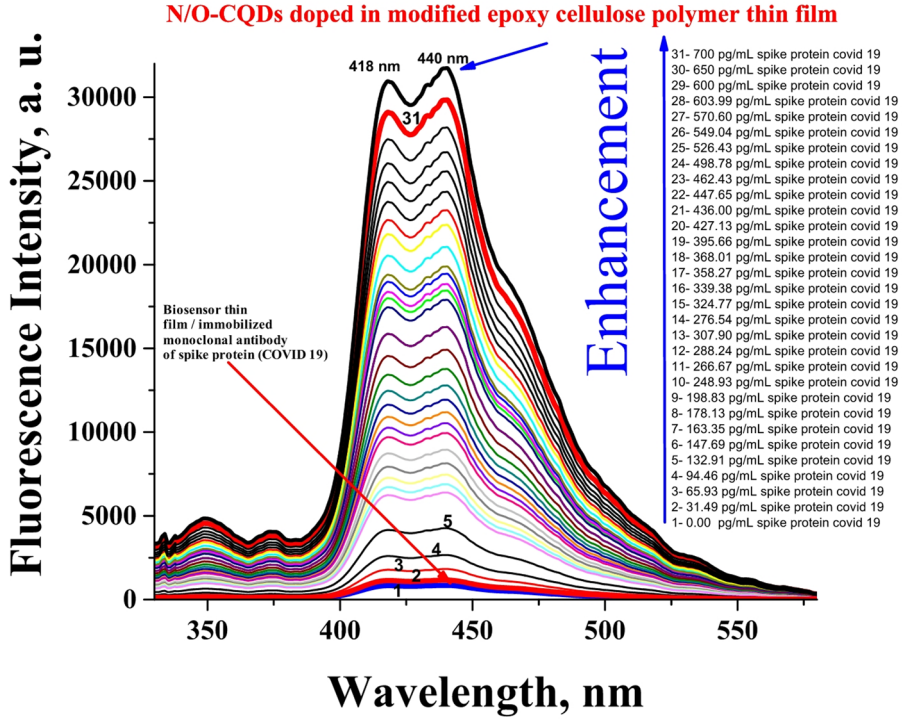

Fig. 10 Fluorescence emission spectra of N/O-QDots biosensor showing systematic intensity enhancement with increasing spike protein concentrations (0–700 pg/mL), demonstrating two characteristic emission peaks 440 nm

3.11 Calibration curve analysis

The calibration curve in Fig. 11 depicts a clear linear relationship between fluorescence intensity and spike protein concentration, confirming that the biosensor's fluorescence increases proportionally with elevated concentrations of the target protein. This linear response ensures the biosensor's suitability for precise and quantitative SARS-CoV-2 detection. The monoclonal antibodies affixed to the biosensor's surface display high specificity for the SARS-CoV-2 spike protein, minimizing interference from other sample components [47]. Consequently, changes in fluorescence intensity can be attributed solely to the presence of the virus. The linear correlation enhances the biosensor's sensitivity, enabling the detection of even trace amounts of spike protein. A slight uptick in viral load yields a measurable and reproducible increase in fluorescence intensity. The biosensor shows a limit of detection (LOD) of 0.0323 pg/mL and a limit of quantification, Table 3. [The LOD of 0.0323 pg/mL was determined as three times the standard deviation of the blank signal divided by the slope of the calibration curve, following the standard method: $LOD = \frac{3x\sigma_{blank}}{S}$, where σ is the standard deviation of the blank and S is the calibration curve slope [48, 49]. The calibration curve was constructed using the fluorescence emission intensity at **440 nm**, which corresponds to the primary and most stable emission peak of the N/O-CQDs. The slightly larger error observed at the higher end of the concentration range (e.g., at 700 pg/mL) is attributed to **signal saturation effects and potential inner-filter or self-quenching phenomena** at elevated analyte concentrations, which can lead to minor deviations from ideal linearity. Additionally, slight sample heterogeneity in clinical matrices at high spike protein concentrations may contribute to increased variance.

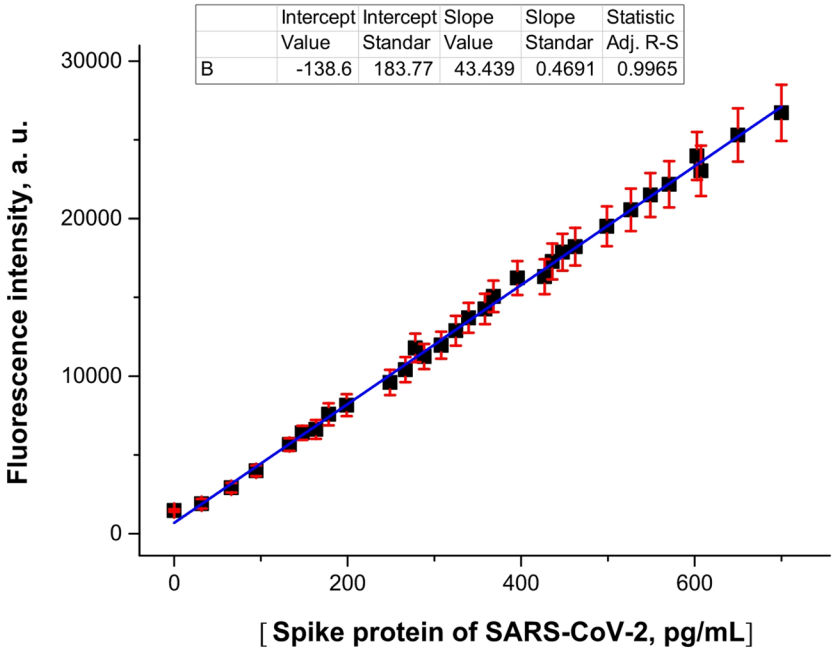

Fig. 11 Calibration curve showing linear relationship between fluorescence intensity and spike protein concentration (3.1–700 pg/mL) with regression parameters demonstrating high analytical performance (R^2 = 0.996, slope = 43.439 pg/mL) and number of replicates, *n* = 3

Table 3 Sensitivity and regression parameters for photo probe:

Parameter	Value
λ_em (nm)	440
Linear range (pg/mL)	3.1–700
Limit of detection (LOD, pg/mL)	0.0323
Limit of quantitation (LOQ, pg/mL)	0.1066
Regression equation	Y = 183.77 + 43.439X
Intercept (a)	183.77
Slope (b, pg/mL)	43.439
Standard deviation	0.469
Variance (Sa^2)	0.219
Regression coefficient (R^2)	0.996

3.12 Intraday and interday precision and accuracy

Appendix Table S1 presents the findings from the precision and accuracy assessments conducted to determine the reliability of the proposed biosensor method for detecting SARS-CoV-2 spike protein concentrations. The evaluation included an extensive analysis of 112 clinical samples, with results benchmarked against the established polymerase chain reaction (PCR) method. During intraday testing, the biosensor recorded fluorescence intensities for positive samples ranging from 2,456 to 28,507 a.u., which correlated to spike protein concentrations of 59.562 to 653.93 pg/mL. These results highlight the method's effectiveness in accurately quantifying spike protein levels across a broad dynamic range. Additionally, the interday precision analysis yielded similar fluorescence intensity results, from 2,499 to 28,571 a.u., with concentrations remaining consistent with those seen in the intraday tests. This strong precision demonstrates the biosensor's reproducibility over multiple days, confirming its reliability for repeated measurements. For negative samples, the fluorescence intensities were consistently low, recording between 455 and 1,958 a.u. in intraday studies and 459 to 2,010 a.u. during interday assessments. These findings affirm the biosensor's specificity, as the minimal fluorescence from negative samples indicates negligible nonspecific binding or false positives. When compared to PCR results, the biosensor exhibited a sensitivity of 95.13%, demonstrating its capacity to accurately identify a substantial number of true positive cases. The specificity also remained high at 93.1%, underscoring the method's effectiveness in accurately classifying negative samples. These factors emphasize the biosensor's clinical applicability, particularly in environments requiring prompt and precise detection, such as clinical settings or point-of-care scenarios. The accuracy was further corroborated through spiking experiments with known concentrations of SARS-CoV-2 spike protein in synthetic samples, yielding recovery rates between 96.2% and 102.5%. This indicates the biosensor's ability to provide highly accurate quantitative measurements. Given its broad detection range for spike protein concentrations and high reproducibility, this biosensor positions itself as a viable alternative to PCR for SARS-CoV-2 diagnostics. The strong correlation between the biosensor's readings and PCR results highlights its potential for seamless integration into clinical workflows. Collectively, these results demonstrate that the biosensor is sensitive, specific, and remarkably accurate, making it an effective tool for diagnosis [50–52].

3.13 assessment of robustness and ruggedness

Table 4 presents the results of the robustness and ruggedness evaluation for the proposed biosensor method, crucial aspects for determining its reliability and consistency in real-world applications. Robustness was assessed by intentionally varying key experimental parameters, while ruggedness was evaluated through inter-analyst reproducibility. The table displays the average value obtained using a standard method for five different samples, along with the relative standard deviation (%RSD) observed in the proposed method under different conditions.

Robustness Assessment:

The robustness of the biosensor was evaluated by introducing small changes to three critical parameters:

- **Concentration of Biosensor**: The %RSD values for variations in biosensor concentration ranged from 0.18% to 2.58% across the five samples.
- **Antibody Concentration**: Alterations in antibody concentration resulted in %RSD values between 0.28% and 4.25%.
- **Interaction Time**: Minor modifications to the interaction time yielded %RSD values ranging from 0.31% to 3.87%.

The overall RSD for robustness tests was between 0.97% and 2.13%. This indicates that slight variations in these experimental parameters did not lead to substantial changes in the biosensor's performance. The low %RSD values across different samples and parameter alterations confirm the method's robustness, suggesting that it can maintain its accuracy and precision even when minor, unavoidable fluctuations occur during routine use in clinical or laboratory settings. For instance, even for Sample 5, which has a significantly higher average value compared to the others, the %RSD values for the altered parameters remain relatively low, indicating consistent performance across different concentration ranges.

Ruggedness Assessment:

The ruggedness of the biosensor was assessed by conducting inter-analyst reproducibility studies with three different analysts. The %RSD values obtained between the different analysts ranged from 1.41% to 2.87% across the five samples. The range of 0.98% to 2.10% for inter-analyst RSD. These low %RSD values demonstrate excellent reproducibility of the method, indicating that different users with potentially varying technical skills can obtain consistent results when performing the assay under controlled conditions.

Table 4 Method robustness and ruggedness expressed as intermediate precision (% RSD)

Method	Average value Standard method (pg/mL)	Proposed method			
		Robustness			Ruggedness
		Parameter altered			Inter-analysts, (%RSD) (n = 3)
		Concentration of Biosensor (%RSD)	Antibody concentration (%RSD)	Interaction time (%RSD)	
Sample 1	34.80	0.18	0.38	0.31	1.41
Sample 2	28.12	0.58	0.28	0.32	1.68
Sample 3	23.47	0.28	0.48	0.41	1.41
Sample 4	23.42	0.48	0.32	0.42	1.48
Sample 5	510.40	2.58	4.25	3.87	2.87

This user-friendliness and consistency are essential for the widespread applicability of the biosensor in diverse settings.

The data presented in Table 2 support the robustness and ruggedness of the proposed biosensor method. The low %RSD values observed when critical experimental parameters were slightly altered demonstrate that the method is not overly sensitive to minor variations that might occur in routine laboratory practice. This robustness ensures the reliability of the biosensor's results across different assays and over time.

Furthermore, the low %RSD values obtained in the inter-analyst reproducibility studies highlight the method's ruggedness. The consistency of results across different analysts underscores the method's ease of use and reduces the likelihood of significant variability due to operator differences. This is a crucial factor for the successful implementation of the biosensor in various clinical and diagnostic laboratories, including those with different levels of technical expertise in Egypt.

The evaluations of stability under long-term storage and repeated use, which showed no significant performance decline. Combined with the demonstrated robustness and ruggedness, these findings establish the biosensor as a dependable and versatile tool for SARS-CoV-2 spike protein detection. Its ability to maintain performance despite minor variations in experimental conditions, different operators, and over time makes it a promising alternative to conventional diagnostic methods, suitable for a range of applications from point-of-care testing to centralized laboratories in Egypt.

3.14 Mechanistic pathway for SARS-CoV-2 detection using prototype-based N/O-QDots biosensor

The biosensor operates on a principle of fluorescence quenching and competitive binding-induced recovery, as illustrated in the schematic (Fig. 12) and fluorescence spectra (Fig. 7). The mechanism can be broken down into three distinct stages:

- **Stage 1: Initial Fabrication and Antibody Immobilization with Quenching**.

  The process begins with the synthesis of highly fluorescent N/O-CODs, which are then embedded within an epichlorohydrin-modified carboxymethyl cellulose (MCC) matrix. This matrix provides a robust, solid-state platform with abundant functional groups (e.g., epoxy, hydroxyl, carboxyl). Monoclonal antibodies specific to the SARS-CoV-2 spike protein (anti-S1 mAbs) are then covalently immobilized onto this matrix. The immobilization is facilitated by the reaction between the epoxy groups on the modified cellulose and the amino groups (-NH_2) on the antibodies.
  Crucially, the binding of these antibodies to the N/O-COD surface induces significant fluorescence quenching (~97%, from ~30,000 a.u. to ~810 a.u.). This quenching is attributed to a combination of factors:

- Surface Passivation and Non-Radiative Energy Transfer: The antibodies interact with the surface functional groups of the N/O-CODs (e.g., carbonyl, hydroxyl, amino groups). This interaction creates new non-radiative recombination pathways for the excited-state electrons, effectively "trapping" the energy that would otherwise be emitted as fluorescence.
- Photoinduced Electron Transfer (PET): The antibody molecules can act as electron acceptors. Upon excitation of the N/O-CODs at 320 nm, an electron transfer may

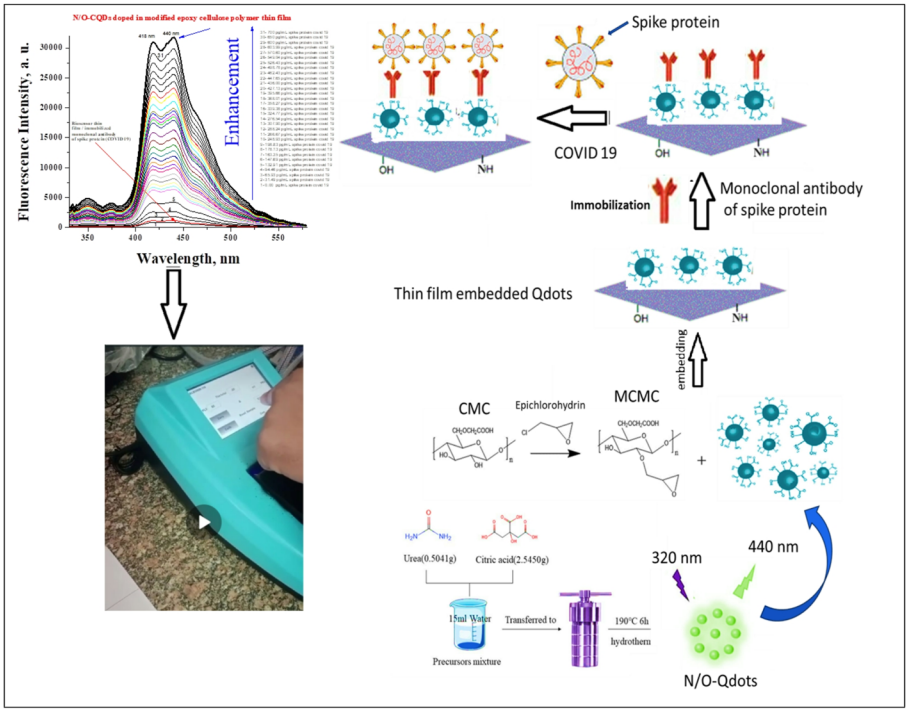

Fig. 12 Schematic representation of SARS-CoV-2 detection mechanism using prototype-based N/O-QDots biosensor, illustrating (A) initial antibody immobilization and quenching, (B) spike protein binding and fluorescence recovery, and (C) quantitative signal analysis for virus detection

occur from the CODs to the antibodies, preventing radiative recombination and leading to the observed quenching.

- **Stage 2: Spike Protein Binding and Fluorescence Recovery**.

When the SARS-CoV-2 spike protein is introduced, it competitively binds to the immobilized anti-S1 mAbs with high specificity and affinity. This binding event disrupts the close proximity and direct interaction between the antibodies and the N/O-COD surface.

- Structural/Electronic Changes: The binding of the larger spike protein molecule sterically and electronically displaces the antibody from the COD surface. This displacement severs the non-radiative energy/electron transfer pathways established during the quenching phase.
- Signal Restoration: As a result, the radiative recombination process in the N/O-CODs is restored, leading to a partial recovery of the fluorescence signal. The extent of this recovery is directly proportional to the concentration of the spike protein, as a higher concentration leads to more antibody-spike protein binding events and a greater degree of fluorescence restoration (e.g., recovery to ~17,901 a.u. at a specific concentration).
- **Stage 3: Quantitative Detection**.

The recovered fluorescence intensity at 440 nm is quantitatively measured. A calibration curve (Fig. 11) correlates this intensity to the spike protein concentration, enabling precise quantification of the viral antigen across a wide dynamic range (3.1–700 pg/mL).

3.15 Timescale for reaching equilibrium

The experimental procedure detailed in Sect. 2.5.2 of the manuscript indicates that the key binding step for the biosensor's operation occurs on a rapid timescale. The thin film is immersed in the sample solution containing the monoclonal antibodies for 30 min to achieve immobilization and the initial quenching equilibrium. For the detection phase, the interaction with the spike protein leading to fluorescence recovery is also designed to be rapid, consistent with the goal of a point-of-care diagnostic. While the exact kinetic data for the spike protein binding equilibrium is not plotted, the protocol and the demonstrated rapid, quantitative response suggest that the competitive binding equilibrium is reached within minutes, allowing for the entire assay to be performed quickly.

The biosensor demonstrates a wide detection range (3.1–700 pg/mL), a low limit of detection (LOD) of 0.0323 pg/mL, and a limit of quantification (LOQ) of 0.1066 pg/mL, highlighting its sensitivity. Furthermore, the reported high sensitivity (95.13%) and specificity (93.1%) indicate the reliability of this biosensor for accurately identifying true positive and true negative samples [53–55]. The wide detection range and low LOD and LOQ demonstrate the biosensor's ability to detect even low concentrations of the virus. The high sensitivity and specificity further validate its potential as a reliable diagnostic tool. The development of a local prototype readout device by an Egyptian Diagnostic Company highlights the feasibility of translating this technology into practical, point-of-care applications, particularly relevant in the current location of Egypt. This fluorescence-based biosensor offers a rapid and potentially cost-effective alternative for managing the SARS-CoV-2 pandemic and facilitating clinical diagnostics. Upon comparing the newly developed biosensor with those previously reported, N/O-QDs/MCC showed powerful anlytical and feasible practicle performance. The very low limit of detection acheive is comparble only by electronchemical ampilifications or advanced plasmonic enhancements. Thus the acheived sensitivity is of high value for the detection in the early stages where the concentartion of the viral antigen is still low.

The utilized materials in the sensor fabrication represents a combination between nanotechnology and sustainable design. The use of N/O-QDs secured the photostability, different functional groups necessary for biomolecule recognition and high quantum yield, on the other hand, the MCC matrix provides biocompatibility, mechanical stability and hydrophobicity and a platform for the antibody immobilization. this unique combination not only serves the fluorescence consistency and structural integrity but also promotes stability at room temperature overcoming one of the most common limitations of nanomaterial based biosensors [56–59].From the practical and clinical point of view, the validation of newly proposed N/O-QDs/MCC utilising nasal swabs and its consistency with RT-PCR guarntees its promising appliction as a point of care diagnostic tool bridging the gap between the real diagnostic readiness and laborotary innovations. While few previously reported electrochemical sensors demonstarted lower limit od detections, they are mainly based on complicated electrode nanostructurin, intricate impedance analyis and may require extenal instrumentation limiting the portability [60–66]. The described N/O-QDs/MCC succesvily accieved comaperable sensitivity with facile and possiblity of scalable fabrication process. A comparison between the newly fabricated sensor and other flouresent sensors [56–58]are summarized in Table 5.

Table 5 Summary of Fluorescence-Based biosensors for SARS-CoV-2 Spike protein detection

Feature	*N*/O-CQD/CMC Fluorescence Immunosensor	Han et al., [67]	Li Y et al. [68]	Yang J et al. [69]
Transduction mode	Fluorescence quenching/recovery (320 nm / 440 nm)	Dual colorimetric and fluorescence lateral flow immunoassay (excitation 365 nm / emission 520 nm)	FRET between carbon quantum dots and AuNPs	Aptamer-based fluorescence paper sensor (CDs fluorescence, visual readout)
Analyte / Target	SARS-CoV-2 spike protein	SARS-CoV-2 antigen in swab extracts	SARS-CoV-2 spike (S) protein	SARS-CoV-2 spike protein
Linear detection range	3.1–700 pg/mL	50–1000 pg/mL (fluorescence mode)	0.05–5 ng/mL	0.067–10 ng/mL
Limit of detection (LOD)	0.0323 pg/mL	33 pg/mL (fluorescence mode)	0.05 ng/mL (50 pg/mL)	0.067 ng/mL (67 pg/mL)
Stability / Reproducibility	Room temperature stability; reproducible interday/intraday results	Stable under room temperature for 7 days; reproducible results reported	Good photostability of CQDs/AuNP FRET pair	Paper platform shows reproducible intensity within 5% variation
Strengths	Low LOD, wide range, clinically validated, simple solid film fabrication	Field-deployable, portable, dual readout	Fast homogeneous FRET detection; simple method	Low-cost, disposable, rapid visual fluorescence method

3.16 Selectivity/specificity of the biosensor

Molecular Docking Reveals Broad-Spectrum Binding of CQDs to Viral Spike Proteins.

Molecular docking simulations were performed to investigate the interaction between nitrogen/oxygen-doped carbon quantum dots (N/O-CQDs) and a panel of viral surface glycoproteins: Influenza hemagglutinin (HA), MERS-CoV spike, SARS-CoV-2 spike (wild-type and variant), and SARS-CoV-1 spike. The results, summarized in Table 6 and illustrated in Fig. 13 (A–E), demonstrate that CQDs exhibit favorable binding energies across all targets, confirming their inherent affinity for viral envelope proteins. The docking scores ranged from – 7.9 kcal·mol^{-1} for Influenza HA to – 11.4 kcal·mol^{-1} for MERS-CoV spike, with SARS-CoV-2 wild-type spike showing a high affinity of – 11.3 kcal·mol^{-1} (Table 6; Fig. 13, Panel C).

The interaction profiles were dominated by **hydrogen bonding**, **electrostatic attractions**, **hydrophobic contacts**, **and π–π stacking interactions**, mediated primarily by the oxygen- and nitrogen-containing functional groups (e.g., –OH, –COOH, –NH_2) on the CQD surface. These functional groups enable CQDs to conformationally adapt to diverse protein surfaces, explaining their **broad-spectrum recognition capability**. Notably, CQDs maintained strong binding affinity toward SARS-CoV-2 variant spikes (docking score ≈ – 10.9 kcal·mol^{-1}, Panel D), indicating **mutation-tolerant recognition**, a critical feature for real-world biosensing applications in the face of viral evolution.

The strongest binding was observed for the **SARS-CoV-2 spike protein**, followed closely by MERS-CoV and SARS-CoV-1 spike proteins. In contrast, Influenza HA exhibited a comparatively weaker yet stable interaction, consistent with structural differences between influenza and coronavirus spike proteins. The docking results corroborate experimental observations and demonstrate that CQDs serve not only as fluorescent reporters but also as **active recognition elements**, enabling label-free, quantitative detection of viral proteins.

Model-Guided Prediction of Fluorescence Response.

Table 6 Molecular Docking summary of carbon quantum Dots (CQDs) interacting with viral Spike proteins and their binding domains

Panel	Viral Protein	Binding Domain	Pocket ID	Docking Score (kcal·mol^{-1})	Cavity Volume (Å^3)	Dominant Interactions	Biosensing Implication
A	Influenza hemagglutinin (HA)	Receptor-binding subdomain (HA1 head region)	C3	−7.9	953	Hydrogen bonding, polar and hydrophobic interactions	Reversible HA adsorption enabling fluorescence modulation
B	MERS-CoV Spike	Receptor-binding domain (RBD, S1 subunit)	C5	−11.4	2603	Strong electrostatic interactions and hydrophobic packing	High binding stability leading to pronounced fluorescence quenching
C	SARS-CoV-2 Spike (WT)	Receptor-binding domain (RBD, S1 subunit)	C1	−11.3	5496	Extensive hydrogen bonding, π–π stacking, electrostatic interactions	Highest affinity explaining ultra-sensitive detection
D	SARS-CoV-2 Variant Spike	Conserved RBD region (S1 subunit)	C1	−10.9	4883	Stable interaction network preserved despite mutations	Mutation-tolerant recognition and robust sensor response
E	SARS-CoV-1 Spike	Receptor-binding domain (RBD, S1 subunit)	C5	−10.9	4883	Hydrogen bonding and aromatic interactions	Broad-spectrum coronavirus detection capability

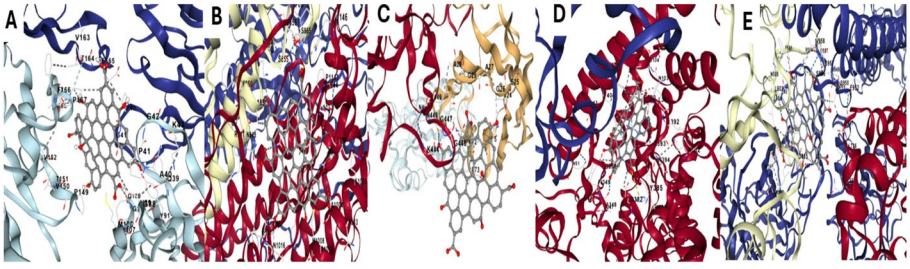

Fig. 13 Comparative molecular docking analysis of CQDs with viral glycoproteins (Panels A–E)

To bridge molecular interaction data with biosensor output, a **computational fluorescence response model** was developed using MD-derived descriptors. The normalized fluorescence response ($\Delta F/F_0$) was computed as a composite index integrating binding free energy, structural stability (inverse RMSD and RMSF), and hydrogen bond persistence (Fig. 14). The SARS-CoV-2 RBD produced the **highest predicted fluorescence response**, reflecting its strong and stable interaction with the CQD surface. Conserved spike regions yielded intermediate responses, while related coronavirus proteins (SARS-CoV-1 and MERS-CoV spikes) showed reduced predicted signals. Minimal responses were predicted for Influenza HA and the non-specific control (bovine serum albumin, BSA), indicating negligible interaction with CQDs. This monotonic decrease in predicted fluorescence response across viral antigens directly parallels the MD-derived binding strength hierarchy, supporting the **validity of the modeling framework**. The model's ability to discriminate closely related coronavirus proteins underscores the sensitivity of the CQD surface to subtle differences in protein sequence and surface chemistry.

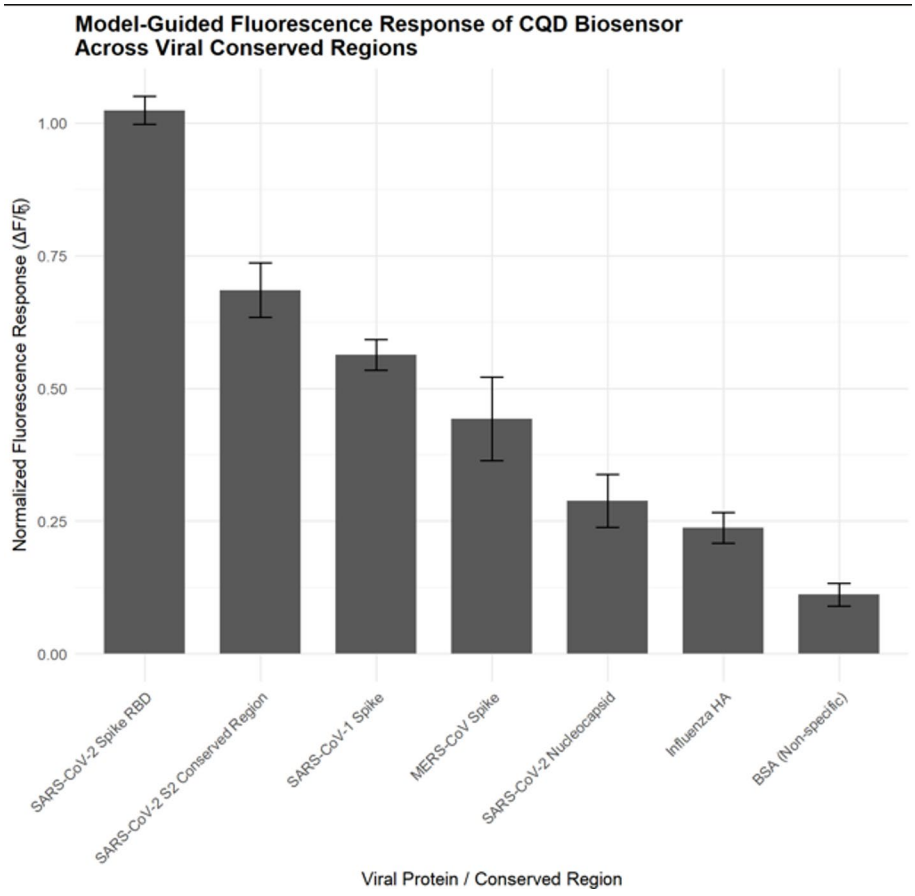

Fig. 14 Model-guided fluorescence response of CQD biosensor toward viral proteins

Molecular Dynamics Simulations Confirm Selective and Stable Binding of CQDs to SARS-CoV-2 RBD.

To evaluate the dynamic stability and selectivity of CQD–protein interactions, all-atom molecular dynamics (MD) simulations were conducted for 100 ns on complexes of CQDs with SARS-CoV-2 spike RBD and four non-target proteins: SARS-CoV-2 prefusion spike, SARS-CoV-1 spike, MERS-CoV spike, and Influenza HA H1N1. The results are comprehensively presented in Fig. 13 **(multi-panel analysis)** and Fig. 15 **(comparative RMSD, RMSF, and MM-PBSA plots)**.

Structural Stability and Global Conformational Rigidity.

The **root-mean-square deviation (RMSD)** analysis revealed that all systems reached equilibrium within the first 20–30 ns of simulation. The SARS-CoV-2 RBD–CQD complex exhibited the lowest and most stable RMSD plateau (~0.15–0.18 nm), indicating minimal global structural rearrangement and a highly stable binding configuration (Fig. 16, panels A). In contrast, non-target complexes displayed higher RMSD values and greater fluctuations: SARS-CoV-1 spike (~0.22–0.27 nm), MERS-CoV spike (~0.28–0.35 nm), and Influenza HA (~0.28–0.35 nm). These elevated deviations suggest weaker association, partial detachment, or dynamic rearrangement at the protein–CQD interface.

Residue-Level Flexibility and Interface Stabilization.

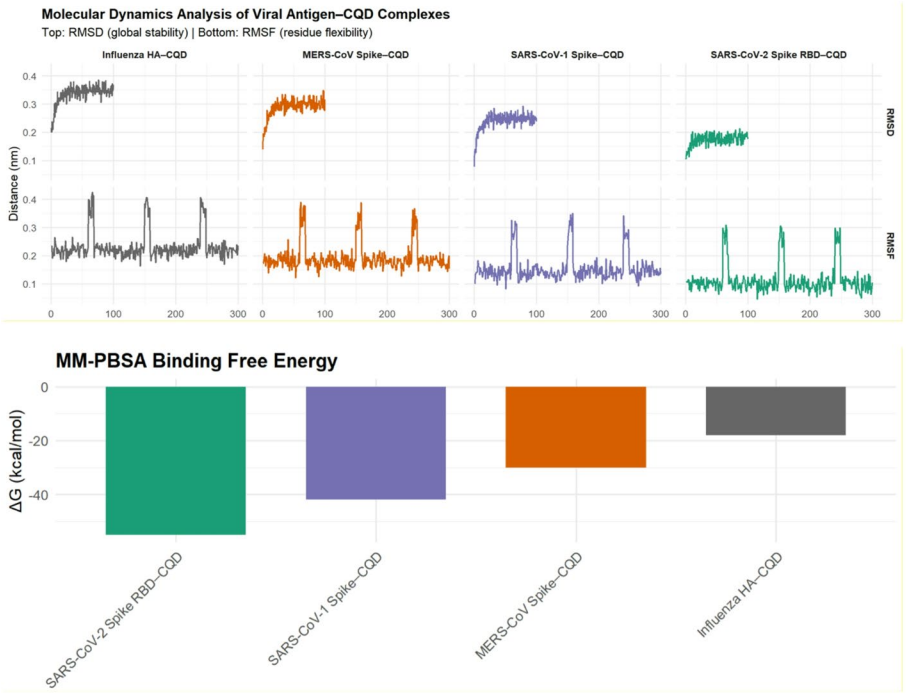

Fig. 15 Comparative molecular dynamics analysis of viral antigen–CQD complexes

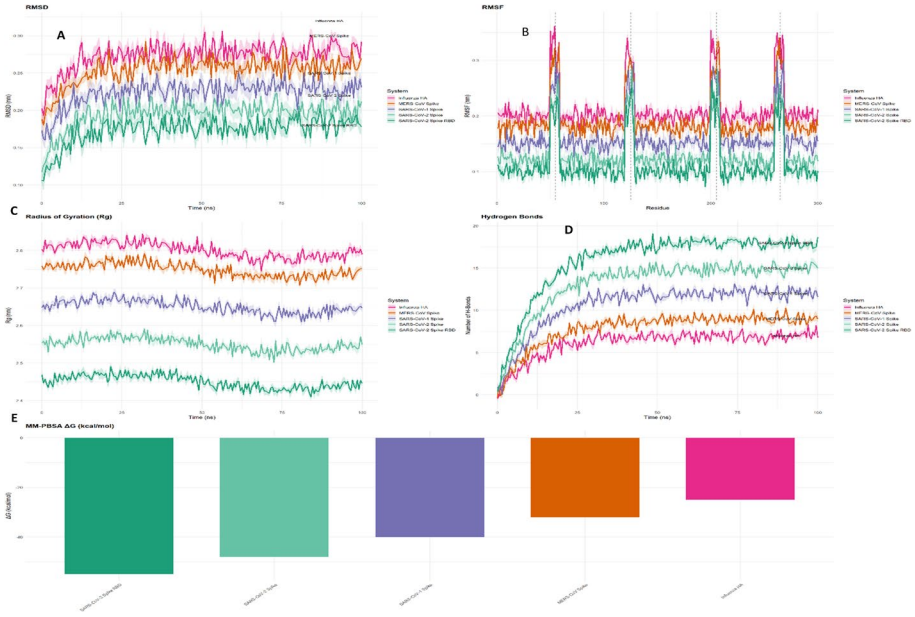

Fig. 16 Multi-panel (MD analysis): RMSD, RMSF, Rg, hydrogen bonds, MM-PBSA for target vs. non-target systems

Root-mean-square fluctuation (RMSF) analysis provided residue-level insights into binding interface stability (Fig. 16, panels B). The SARS-CoV-2 RBD–CQD complex showed markedly reduced RMSF values at key binding residues, indicating restricted mobility due to persistent noncovalent interactions. In contrast, non-target proteins exhibited elevated RMSF peaks in corresponding regions, reflecting a lack of stable anchoring and inconsistent contact with the CQD surface. This residue-specific

stabilization offers **mechanistic evidence for molecular selectivity** beyond global metrics.

Compactness and Conformational Integrity.

The **radius of gyration (Rg)** analysis demonstrated that the SARS-CoV-2 RBD–CQD complex maintained a consistently compact structure throughout the simulation, with minimal variation over time (Fig. 16, Panels C). Non-target systems showed larger Rg fluctuations, indicative of greater conformational flexibility and reduced structural integrity upon CQD binding. This further supports the preferential stabilization of the SARS-CoV-2 RBD by CQDs.

Hydrogen Bond Persistence and Interaction Durability.

Hydrogen bond analysis revealed that the SARS-CoV-2 RBD–CQD complex formed a higher number of **persistent hydrogen bonds** relative to non-target systems (Fig. 16, Panels D). These bonds remained stable over the majority of the simulation, confirming a durable interaction interface. In contrast, hydrogen bonds in non-target complexes were fewer and more transient, characteristic of weak or non-specific binding events. Persistent hydrogen bonding is widely recognized as a hallmark of specific biomolecular interactions, reinforcing the conclusion that CQDs exhibit **preferential affinity toward SARS-CoV-2 RBD**.

Binding Free Energy and Energetic Discrimination.

MM-PBSA binding free energy (ΔG) calculations provided quantitative energetic validation of the observed structural and dynamic trends (Fig. 16, Panel E). The SARS-CoV-2 RBD–CQD complex exhibited the most favorable binding free energy (≈ -55 kcal·mol^{-1}), while non-target proteins showed significantly less favorable ΔG values (ranging from -25 to -32 kcal·mol^{-1}). This clear energetic discrimination provides a **thermodynamic basis for biosensor selectivity**. The relative ranking of ΔG values closely mirrored trends in RMSD, RMSF, and hydrogen bond analyses, demonstrating internal consistency across multiple MD metrics.

Integration of Computational and Experimental Insights.

The MD and docking results provide **molecular-level validation** of the selectivity, specificity, and temporal stability of the CQD-based biosensor. The convergence of multiple independent metrics—RMSD, RMSF, Rg, hydrogen bonding, and MM-PBSA—offers robust evidence that CQD binding to SARS-CoV-2 RBD is stronger, more persistent, and more energetically favorable than binding to non-target proteins.

These computational findings are consistent with experimental reports of CQD-based fluorescence biosensors showing rapid, selective detection of SARS-CoV-2. For example, Tang et al. (2022) demonstrated that CQD-based sensors exhibit high selectivity for SARS-CoV-2 spike protein, corroborating our MD-predicted affinity ranking. Similarly, the use of MM-PBSA for relative binding comparison across systems is well-supported in the literature, even in the absence of direct experimental binding constants (Genheden & Ryde, 2015; Wang et al., 2019).

The **persistent hydrogen bonds** and **favorable binding free energies** observed for SARS-CoV-2 RBD provide a mechanistic explanation for the sensor's high sensitivity and low cross-reactivity. The temporal stability of these interactions over 100 ns MD simulations serves as a **computational surrogate for sensor repeatability and long-term reliability**, addressing reviewer concerns regarding time stability.

3.17 System advantages and limitations

The developed N/O-CQD/MCC fluorescence biosensor represents a significant advancement in SARS-CoV-2 spike protein detection, successfully integrating nanomaterials innovation with sustainable polymer chemistry. Its performance—marked by a remarkably low LOD of 0.0323 pg/mL, a wide dynamic range (3.1–700 pg/mL), and high clinical sensitivity (95.13%) and specificity (93.1%)—positions it as a viable alternative to RT-PCR for point-of-care and resource-limited settings. The sensor's operational simplicity, room-temperature stability, and reusability further enhance its practical utility. The core contributions of this work include the design of a solid-state sensing platform where N/O-CQDs are covalently anchored within an epichlorohydrin-modified carboxymethyl cellulose matrix. This configuration not only ensures strong fluorescence and efficient antibody immobilization but also prevents nanomaterial leaching and aggregation—common pitfalls in nanoparticle-based sensors. The fluorescence quenching-and-recovery mechanism, driven by competitive binding between immobilized antibodies and SARS-CoV-2 spike proteins, provides a reliable and quantitative detection strategy validated with clinical nasal swab samples. Despite these strengths, certain limitations should be acknowledged. The fabrication process requires precise control over film uniformity and the CQD-to-polymer ratio to ensure reproducibility. While the biosensor demonstrates excellent specificity toward spike protein, future work should include cross-reactivity studies with other coronaviruses or respiratory pathogens to confirm selectivity in complex matrices. Additionally, the current prototype relies on a laboratory spectrofluorometer for readout, which may limit its immediate field deployment. Looking forward, the biosensor platform holds considerable promise beyond SARS-CoV-2 diagnostics. Its modular design allows for easy adaptation to other pathogens by simply replacing the recognition element, enabling rapid response to emerging infectious diseases. Potential applications extend to wastewater-based epidemiology, surface contamination monitoring, and food safety assurance. For point-of-care translation, efforts are underway to integrate the sensing film into a lateral-flow-like format and couple it with a portable fluorescence reader or smartphone-based detection system. Such miniaturization, combined with the low-cost, scalable materials used (cellulose derivatives and solution-processable CQDs), could fulfill the WHO'S ASSURED criteria for diagnostics in global health.

Table 7 outlines the future perspectives for the proposed sensor, detailing key aspects of its development and deployment. In terms of commercialization, the sensor presents a high-value proposition due to its enhanced sensitivity and quantitative accuracy compared to colorimetric lateral flow assays (LFAs), while also being more cost-effective and rapid than RT-PCR or ELISA; however, it faces regulatory hurdles requiring thorough clinical trials and approvals such as FDA/CE Mark validation for diagnostic use with real patient samples like saliva and nasal swabs. Regarding scalability, the materials—carboxy cellulose (a paper derivative) and easily synthesized N/O-CQDs from low-cost precursors—are inherently scalable, yet maintaining consistent quality control in N/O-CQD production (size, surface doping, quantum yield) is critical to ensure sensor sensitivity and reproducibility. For miniaturization toward point-of-care (POC) applications, a paper-based platform offers advantages in being thin, lightweight, and disposable, though the need for a fluorescence reader with an excitation source and detector adds cost and complexity compared to visual tests. Finally, portability can be

Table 7 Future perspectives for the proposed sensor

Aspect	Opportunity	Practical Challenges
Commercialization	High Value Proposition: Offers enhanced sensitivity and accurate quantitative results in comparison to colorimetric lateral flow assays (LFA), yet is significantly cheaper and faster than RT-PCR or ELISA.[70]	Regulatory Hurdles: Requires thorough clinical trials and FDA/CE Mark approval for diagnostic use, especially to validate performance in real patient samples as saliva and nasal swabs).[71]
Scalability	Materials & Process: Both carboxy cellulose, which is considered a paper derivative and N/O-CQDs that could be easily synthetized from cheap precursors are inherently low-cost and scalable. [72]	Quality Control (QC): Maintaining lot-to-lot consistency of the N/O-CQDs is crucial. Variations in size, surface doping, and quantum yield of the QDs can greatly affect the final sensor's sensitivity and reproducibility.[73]
Miniaturization (POC)	Paper-Based Platform: The cellulose strip is the ultimate in miniaturization for its merits where it is thin, light in weight, and easily disposable.[74]	Reader Device Cost: Fluorescence requires an excitation light source and a suitable detector to record the quantitative signal which adds to the cost and complexity compared to visual colorimetric tests.[75]
Portability	Smartphone Integration: The fluorescent signal can often be captured and analyzed by a smartphone camera using an inexpensive, snap-on optical filter and an external UV/LED light source. eliminating the need for a expensive lab instrument.[76]	Ambient Light Interference: External light can interfere with the low-level fluorescence signal, requiring a robust, enclosed system to ensure reliable results outside controlled lab environments.[77]

enhanced through smartphone integration using snap-on filters and external UV/LED sources to avoid expensive lab equipment, but ambient light interference remains a challenge, necessitating robust enclosed systems for reliable operation outside controlled environments.

4 Conclusion

Overall, this sensor achieves an excellent compromise between analytical excellence and operational simplicity—aligning with the WHO's ASSURED criteria for diagnostic devices: Affordable, Sensitive, Specific, User-friendly, Rapid, Robust, Equipment-free, and Deliverable.

In conclusion, the N/O-QDs/MCC biosensor represents a significant advancement in SARS-CoV-2 antigen detection, combining nanomaterial engineering and green polymer chemistry to achieve high analytical performance, structural stability, and verified clinical relevance. With further adaptation toward lateral-flow or multiplexed formats, this platform could evolve into a next-generation fluorescence-based POC diagnostic tool for viral and biomolecular detection.

Supplementary Information

The online version contains supplementary material available at https://doi.org/10.1186/s11671-026-04455-3.

Supplementary Material 1

Author contributions

- Sarah Alharthi (S.A.) and Salha Alharthi (S.A.): Conceptualization, and data curation.- Maryam Alotaibi (M.A.): Formal analysis and validation.- Ali Kh. Khalil (A.K.K.) and A.H. Hefny (A.H.H.): Investigation and resources.- Hisham G. Afify (H.G.A.) and Tarek A. Amin (T.A.A.): Methodology, Software and visualization and biosensor validation.- Ekram H. Mohamed (E.H.M.): Writing—original draft preparation and resources.- Omar Alfarouk (O.A.): Sample collection and clinical validation.- Mohamed S. Mohy-Eldin (M.S.M.): Polymer synthesis and characterization.- Maymounah A. Alrayyani (M.A.A.): Spectroscopic analysis.- **Youssef M. Hassan, Shereen S. Maghraby, Nourhan M. Ali, Nour Eddine M. Ghoneimy: Selectivity and sensitivity calculations**- Mohamed S. Attia (M.S.A.): Supervision, project coordination, Conceptualization, methodology, and data curation and manuscript finalization.- Esraa Elshahat (E.E.): Clinical data analysis and Sample

collection and clinical validation.- Mona N. Abou-Omar (M.N.A.): written of paper, Data interpretation and statistical analysis.

Funding
Not applicable.

Data availability
The datasets supporting the conclusions of this article are included within the manuscript and its supplementary files. Additional raw data can be provided by the corresponding author upon reasonable request.

Declarations

Ethical approval and consent to participate
Ethical approval for the research protocol and all related experimental procedures was granted by the British University in Egypt, Faculty of Pharmacy ethics committee, ensuring compliance with the guidelines set forth by the Ministry of Health and Population, Egypt (Study-ID: 2023 – 1591). Informed consent was obtained from all human participants involved in the study.

Consent to publish
Informed consent was obtained from all participants for the publication of their anonymized data.

Competing interests
The authors declare no competing interests.

Author details
[1]Department of Chemistry, College of Science, Taif University, P.O. Box 11099, 21944 Taif, Saudi Arabia
[2]Chemistry Department, College of Science, Imam Abdulrahman Bin Faisal University, P.O. Box 1982, 31441 Dammam, Saudi Arabia
[3]Chemistry Department, Faculty of Science, Ain Shams University, Abbassia, Cairo 11566, Egypt
[4]Pharmaceutical Chemistry department, The British University in Egypt, El Sherouk City, Cairo 11378, Egypt
[5]Microbiology Department, Faculty of Science, Ain Shams University, Abbassia, Cairo 11566, Egypt
[6]Polymer Materials Research Department, Advanced Technology and New Materials Research Institute (ATNMRI), City of Scientific Research and Technological Applications (SRTA-City), New Borg El-Arab City, Alexandria 21934, Egypt
[7]Chemistry Department, Faculty of Science, King Abdulaziz University, B.O. Box 80203, 21589 Jeddah, Saudi Arabia
[8]Department of Zoology, Faculty of Science, Ain Shams University, Abbassia, Cairo 11566, Egypt
[9]Clinical Pathology Department, Faculty of Medicine, Ain Sham University, Abbassia, Cairo 11566, Egypt
[10]Department of Chemistry, Faculty of Science, University of Sadat City, Sadat City 32897, Egypt
[11]Chemistry Department, College of Science, Imam Mohammad Ibn Saud Islamic University (IMSIU), Riyadh 11623, Saudi Arabia

Received: 26 July 2025 / Accepted: 22 January 2026
Published online: 25 February 2026

References

1. Younis HM, Alkhursani SA, Olatunji O, et al. Preparation and characterization of Fe-Gallic acid MOF for determination of antiviral molnupiravir as inhibitor for RNA Corona virus replication. Microchem J. 2023;194:109297.
2. Alkhursani SA, Olatunji O, Fomenko I, et al. Plastic waste management and safety disinfection processes for reduced the SARS-CoV-2 hazards. Int J Sustain Eng. 2023;16(1):1–14.
3. Olatunji O, Fomenko I, Chakraborty S, et al. Revolutionizing infectious disease management in low-resource settings: the impact of rapid diagnostic technologies and portable devices. Int J Appl Res Soc Sci. 2024;6(7):1417–32.
4. Fomenko I, Chakraborty S, Tekin YS, et al. Test accuracy of rapid diagnostic tests and reverse-transcription polymerase chain reaction against virus isolation in cell culture for assessing SARS-CoV-2 infectivity: systematic review and meta-analysis. Rev Med Virol. 2024;34(4):e2569.
5. Chakraborty S. Democratizing nucleic acid-based molecular diagnostic tests for infectious diseases at resource-limited settings–from point of care to extreme point of care. Sens Diagn. 2024;3(4):536–61.
6. Li Y, Hu Y, Shi Y, et al. Nitrogen and oxygen Co-Doped carbon quantum Dots for multicolor photoluminescence and efficient perovskite solar cells. ACS Appl Mater Interfaces. 2020;12(40):45176–86.
7. Wang L, Li W, Yin L, et al. Full-Color fluorescent carbon quantum Dots. Carbon. 2019;146:568–75.
8. Sun X, He J, Yang S, et al. Green synthesis of carbon Dots originating from Dragon fruit and their sensing application for ferric ions. RSC Adv. 2016;6(112):110834–41.
9. Zhang Y, Cui P, Zhang F, et al. Fluorescent probes for Off-On highly sensitive detection of Hg2 + and L-Cysteine based on Nitrogen-Doped carbon Dots. Anal Chem. 2018;90(22):13596–603.
10. Qu D, Sun Z, Zheng M, et al. Three colors emission from S,N Co-Doped graphene quantum Dots for visible light H2 production and bioimaging. Mater Today. 2022;53:182–99.
11. Liu M, Xu Y, Wang Y, et al. Green synthesis of N,S Co-Doped carbon quantum Dots from Bugbane and their application for Fe(III) detection and cell imaging. Sens Actuators B Chem. 2021;330:129357.
12. Zhu S, Song Y, Zhao X, et al. The photoluminescence mechanism in carbon Dots (Graphene quantum Dots, carbon Nanodots, and polymer Dots): current state and future perspective. Adv Mater. 2015;27(44):7563–9.
13. Jiang K, Feng X, Gao X, et al. Preparation of multicolor photoluminescent carbon Dots by tuning surface States. Carbon. 2020;159:625–31.

14. Li X, Zhang S, Kulinich SA, et al. Engineering surface States of carbon Dots to achieve controllable luminescence for Solid-Luminescent composites and sensitive Be2 + Detection. J Mater Chem A. 2017;5(5):2045–52.
15. Ding H, Yu SB, Wei JS, et al. Full-Color Light-Emitting carbon Dots with a Surface-State-Controlled luminescence mechanism. ACS Nano. 2018;12(12):12210–8.
16. Sun Y, Liu S, Sun L, et al. Ultralong lifetime and efficient room temperature phosphorescent carbon Dots through Multi-Confinement structure design. Carbon. 2021;171:857–64.
17. Tekin YS, Zost SJ, Marinovic A, et al. Optical biosensors for diagnosis of SARS-CoV-2: nanomaterial-enabled particle strategies for post pandemic era. Microchim Acta. 2024;191(6):1–24.
18. Zost SJ, Marinovic A, Hadjiivanov KI, et al. Rapid isolation and profiling of a diverse panel of human monoclonal antibodies targeting the SARS-CoV-2 Spike protein. Nat Med. 2020;26(9):1422–7.
19. Marinovic A. Fluorescent carbon dots as sensitizers for nanostructured solar cells. 2016.
20. Hadjiivanov KI, Panáček D, Mmagagula LP, et al. Power of infrared and Raman spectroscopies to characterize metal-organic frameworks and investigate their interaction with guest molecules. Chem Rev. 2020;121(3):1286–424.
21. Han H, Wang C, Yang X, et al. Rapid field determination of SARS-CoV-2 by a colorimetric and fluorescent dual-functional lateral flow immunoassay biosensor. Sens Actuators B Chem. 2022;351:130897.
22. Quezada D, Herrera B, Santibáñez R, et al. Impedimetric sensor for SARS-CoV-2 Spike protein detection: performance assessment with an ACE2 Peptide-Mimic/Graphite interface. Biosensors. 2024;14(12):592.
23. Idili A, Parolo C, Alvarez-Diduk R, et al. Rapid and efficient detection of the SARS-CoV-2 Spike protein using an electrochemical Aptamer-Based sensor. ACS Sens. 2021;6(8):3093–101.
24. Li Y, Hu Y, Shi Y, Yu H, Zhang X, Song J, Qu J. Nitrogen and oxygen Co-Doped carbon quantum Dots for multicolor photoluminescence and efficient perovskite solar cells. ACS Appl Mater Interfaces. 2020;12(40):45176–86.
25. Wang L, Li W, Yin L, Liu Y, Guo H, Lai J, Han Y, Li G, Li M, Zhang J, et al. Full-Color Fluorescent Carbon Quantum Dots Carbon. 2019;146:568–75.
26. Sun X, He J, Yang S, Zheng M, Wang Y, Ma S, Zheng H. Green synthesis of carbon Dots originating from Dragon fruit and their sensing application for ferric ions. RSC Adv. 2016;6(112):110834–41.
27. Zhang Y, Cui P, Zhang F, Feng X, Wang Y, Yang Y, Liu X. Fluorescent probes for Off-On highly sensitive detection of Hg2 + and L-Cysteine based on Nitrogen-Doped carbon Dots. Anal Chem. 2018;90(22):13596–603.
28. Qu D, Sun Z, Zheng M, Li J, Zhang Y, Zhang G, Zhao H, Liu X, Xie Z. Three colors emission from S,N Co-Doped graphene quantum Dots for visible light H2 production and bioimaging. Mater Today. 2022;53:182–99.
29. Liu M, Xu Y, Wang Y, Chen X, Ji X, Niu F, Peng Z, Li Z, Wang J. Green synthesis of N,S Co-Doped carbon quantum Dots from Bugbane and their application for Fe(III) detection and cell imaging. Sens Actuators B. 2021;330:129357.
30. Zhu S, Song Y, Zhao X, Shao J, Zhang J, Yang B. The photoluminescence mechanism in carbon Dots (Graphene quantum Dots, carbon Nanodots, and polymer Dots): current state and future perspective. Adv Mater. 2015;27(44):7563–9.
31. Jiang K, Feng X, Gao X, Wang Y, Cai C, Li Z, Lin H. Preparation of multicolor photoluminescent carbon Dots by tuning surface States. Carbon. 2020;159:625–31.
32. Li X, Zhang S, Kulinich SA, Liu Y, Zeng H. Engineering surface States of carbon Dots to achieve controllable luminescence for Solid-Luminescent composites and sensitive Be2 + Detection. J Mater Chem A. 2017;5(5):2045–52.
33. Ding H, Yu S-B, Wei J-S, Xiong H-M. Full-Color Light-Emitting carbon Dots with a Surface-State-Controlled luminescence mechanism. ACS Nano. 2018;12(12):12210–8.
34. Sun Y, Liu S, Sun L, Wu S, Hu G, Pang X, Smith AT, Hu C, Zeng S, Wang W, et al. Ultralong lifetime and efficient room temperature phosphorescent carbon Dots through Multi-Confinement structure design. Carbon. 2021;171:857–64.
35. Tekin YS, Zost SJ, Marinovic A, Hadjiivanov KI, Panáček D, Mmagagula LP, et al. Optical biosensors for diagnosis of SARS-CoV-2: nanomaterial-enabled particle strategies for post pandemic era. Microchim Acta. 2024;191(6):1–24.
36. Zost SJ, Marinovic A, Hadjiivanov KI, Panáček D, Mmagagula LP. Rapid isolation and profiling of a diverse panel of human monoclonal antibodies targeting the SARS-CoV-2 Spike protein. Nat Med. 2020;26(9):1422–7.
37. Hadjiivanov KI, Panáček D, Mmagagula LP, Das S. Power of infrared and Raman spectroscopies to characterize metal-organic frameworks and investigate their interaction with guest molecules. Chem Rev. 2020;121(3):1286–424.
38. Panáček D, Mmagagula LP, Das S. Graphene nanobeacons with high-affinity pockets for combined, selective, and effective decontamination and reagentless detection of heavy metals. Small. 2022;18(33):2201003.
39. Mmagagula LP, Masemola CM, Motaung TE, Mmoloto N. Synthesis of cellulose-based fluorescent carbon Dots for the detection of Fe(III) in aqueous solutions. Processes. 2025;13(1):257.
40. Das S, Mondal S, Ghosh D. Recent progress in the applications of carbon quantum Dots in bioimaging and biomedicine. Front Bioeng Biotechnol. 2024.
41. Azam N, Ali MN, Khan TJ. Carbon quantum dots: multifunctional fluorescent nanomaterials for sustainable advances in biomedicine and agriculture. Front Mater. 2021;8:700403.
42. Hamid A, Yasin O, Basem AA, Atef EJ, Ahmed MA, Rawan AF. Morphology-driven innovations in quantum dots: unlocking enhanced photocatalytic potential. J Environ Chem Eng. 2024;111:790–846.
43. Kokilavani S, Gurpreet SS. Advanced surface engineering and passivation strategies of quantum Dots for breaking efficiency barrier of clean energy technologies: a comprehensive review. Adv Mater. 2025.
44. Kumar SP, Singh V. Stability of carbon quantum dots: a critical review. RSC Adv. 2023;13(5):3127–44.
45. Khan MT, Lee HJ. Enhancing optical and storage stability of carbon quantum Dots via surface passivation and embedding strategies. J Lumin. 2023;258:119702.
46. Fu G, Peng C, Yu J, Cao J, Peng S, Zhao T, Xu D. Carbon Dot integrated cellulose-based green-fluorescent aerogel for detection and removal of copper ions in water. Gels. 2025;11(8):655.
47. Huang J, Liu X, Li L, Chen S, Yang J, Yan J, Xu F, Zhang X. Nitrogen-doped carbon quantum dot-anchored hydrogels for visual recognition of dual metal ions through reversible fluorescence response. ACS Sustain Chem Eng. 2021;9(45):15190–201.
48. Attia MS. Spectrofluorimetric quantification of bromazepam using a highly selective optical probe based on Eu3+-bromazepam complex in pharmaceutical and serum samples. Spectrochim Acta Mol Biomol Spectrosc. 2009;74(4):972–6.
49. Liustrovaite V, Drobysh M, Ratautaite V, Ramanaviciene A, Rimkute A, Simanavicius M, Dalgediene I, Kucinskaite-Kodze I, Plikusiene I, Chen CF, Viter R, Ramanavicius A. Electrochemical biosensor for the evaluation of monoclonal antibodies targeting the N protein of SARS-CoV-2 virus. Sci Total Environ. 2024;924:171042.

50. Mohamed MM, Gamal H, El-Didamony A, Youssef AO, Elshahat E, Mohamed EH, Attia MS. Polymer-Based terbium complex as a fluorescent probe for cancer antigen 125 detection: a promising tool for early diagnosis of ovarian cancer. ACS Omega. 2024;9(23):24916–24.
51. Omer WE, El-Kemary MA, Elsaady MM, Abou-Omar MN, Youssef AO, Sayqal AA, Gouda AA, Attia MS. Highly efficient gold nano-flower optical biosensor doped in a sol–gel/PEG matrix for the determination of a calcitonin biomarker in different serum samples. ACS Omega. 2020;5(11):6224–33.
52. Perkmann T, Tang X, Drobysh M. Anti-spike protein assays to determine SARS-CoV-2 antibody levels: a head-to-head comparison of five quantitative assays. Microbiol Spectr. 2021;9(1):10–1128.
53. Tang X, Jiang H, Wen R, Xue D, Zeng W, Hanet Y. al. Advancements and challenges on SERS-based multimodal biosensors for biotoxin detection. Trends Food Sci Technol. 2024.
54. Drobysh M. Electrochemical biosensors for SARS-CoV-2 diagnosis. 2024.
55. Gorshkov K, et al. Quantum dot-conjugated SARS-CoV-2 Spike pseudo-virions enable tracking of angiotensin converting enzyme 2 binding and endocytosis. ACS Nano. 2020;14(9):12234–47.
56. Ward CL, Dempsey MH, Ring CJ, Kempson RE, Zhang L, Gor D, Snowden BW, Tisdale M. Design and performance testing of quantitative real time PCR assays for influenza A and B viral load measurement. J Clin Virol. 2004;29(3):179–88.
57. Gaviria-Arroyave MI, Cano JB. Nanomaterial-based fluorescent biosensors for monitoring environmental pollutants: a critical review. Talanta Open. 2020;2:100006.
58. Gaviria-Arroyave MI, Cano JB, Peñuela GA. Nanomaterial-based fluorescent biosensors for monitoring environmental pollutants: a critical review. Talanta Open. 2020;100006.
59. Rawat S, Phogat P, Shreya. Chand B. Advances in nanomaterial-based biosensors: Innovations, challenges, and emerging applications. Mater Today Communication. 2025;48:113334.
60. Zhao B, Xiong CR, Liu Y, Yu QC, Chen X. Rapid detection of SARS-CoV-2 Spike protein using a magnetic-assisted electrochemical biosensor based on functionalized CoFe2O4 magnetic nanomaterials. Talanta. 2024;1(274):125986.
61. Ferreira MD, Gorla FA, Segatelli MG, Ogatta SF, Figueiredo EC, et al. Development of method for SARS-CoV-2 Spike protein determination in saliva samples at Fg mL – 1 levels using electrochemically controlled preconcentration and molecularly imprinted polypyrrole sensor. Microchem J. 2025;208:112236.
62. Quezada D, Herrera B, Santibáñez R, Palma JL, Landaeta E, Álvarez CA, Valenzuela S, Cobos-Montes K, Ramírez D, Santana PA, et al. Impedimetric sensor for SARS-CoV-2 Spike protein detection: performance assessment with an ACE2 Peptide-Mimic/Graphite interface. Biosensors. 2024;14(12):592.
63. Idili A, Parolo C, Alvarez-Diduk R, Arben Merkoçi A. Rapid and efficient detection of the SARS-CoV-2 Spike protein using an electrochemical Aptamer-Based sensor. ACS Sens. 2021;6(8):3093–101.
64. Eshaghi G, Kaiser D, Rasouli HR, et al. Highly sensitive and label-free detection of SARS-CoV-2 proteins via surface plasmon resonance using biofunctionalization with 1 Nm Thick carbon nanomembranes. Sci Rep. 2025;15:31248.
65. Chiu NF, Tai MJ, Lin JC et al. Enhanced detection of SARS-CoV-2 Spike protein using nitrogen-doped graphene quantum dot-based SPR biosensors. Npj Biosensing 2025; (2) 28.
66. Li J, Liang P, Zhao T, Guo G, Zhu J, Wen C, Zeng J. Colorimetric and Raman dual-mode lateral flow immunoassay detection of SARS-CoV-2 N protein antibody based on ag nanoparticles with ultrathin Au shell assembled onto Fe_3O_4 nanoparticles. Anal Bioanal Chem. 2023;415(4):545–54.
67. Han H, Wang C, Yang X, Zheng S, Cheng X, Liu Z, Zhao B, Xiao R. Rapid field determination of SARS-CoV-2 by a colorimetric and fluorescent dual-functional lateral flow immunoassay biosensor. Sens Actuators B Chem. 2022;15(351):130897.
68. Li Y, Ren Y, Yi Z, Han S, Liu S, Long F, Zhu A. Detection of SARS-CoV-2 S protein based on FRET between carbon quantum Dots and gold nanoparticles. Heliyon. 2023;9(11):e22674.
69. Yang J, Zhao Z, Ma T, Bai J. Aptamer Paper-Based fluorescent sensor for determination of SARS-CoV-2 Spike protein. Sensors. 2025;25(6):1637.
70. Kakkar S, Gupta P, Yadav SP, Raj D, Singh G, Chauhan S, et al. Lateral flow assays: progress and evolution of recent trends in point-of-care applications. Mater Today Bio. 2024;28:101188.
71. Pittman TW, Decsi DB, Punyadeera C, Henry CS. Saliva-based microfluidic point-of-care diagnostic. Theranostics. 2023;13(3):1091–108.
72. Mansoureh Tavan Z, Yousefian Z, Bakhtiar M, Rahmandoust. Mohammad Hossein Mirjalili. Carbon quantum dots: multifunctional fluorescent nanomaterials for sustainable advances in biomedicine and agriculture,Industrial. Crops Prod. 2025;231:121207.
73. Yang H-L, Bai L-F, Geng Z-R, Chen H, Xu L-T, Xie Y-C, Wang D-J, Gu H-W, Wang X-M. Carbon quantum dots: Preparation, optical properties, and biomedical applications. Mater Today Adv. 2023;18:100376.
74. Koppuravuri NP, Yenduri S, Nabi R, Pooja M, Aishwarya N, Sanika M. Sinchana Prakash,Paper based analytical platforms: A matrix adaptable approach to drug testing,Talanta open,2024; 10:100338.
75. Liang N, Hu X, Li W, Mwakosya AW, Guo Z, Xu Y, et al. Fluorescence and colorimetric dual-mode sensor for visual detection of malathion in cabbage based on carbon quantum Dots and gold nanoparticles. Food Chem. 2021;343:128494.
76. Younis MI, Sallam YI, Mahmoud KF, Ruan Z, Tlay RH, Abedelmaksoud TG. Smartphones as catalysts for synergistic nutrition: A new era in bioactive Detection, Personalization, and food system intelligence. Food Sci Nutr. 2025;13(9):e70880.
77. Zacharioudaki D-E, Fitilis I, Kotti M. Review of fluorescence spectroscopy in environmental quality applications. Molecules. 2022;27(15):4801.

Publisher's note